Two-pulse rapid remote surface contamination measurement

Thomas J. Kulp, Scott E. Bisson, Thomas A. Reichardt,
Jeffrey M. Headrick, and Roger L. Farrow

Approved for public release; further dissemination unlimited.

Sandia National Laboratories

Two-Pulse Rapid Remote Surface Contamination Measurement

Thomas J. Kulp, Scott E. Bisson, Thomas A. Reichardt,
Jeffrey M. Headrick, and Roger L. Farrow
Diagnostics and Remote Sensing Department
Sandia National Laboratories
P.O. Box 969
Livermore, CA 94551-0969

Abstract

This project demonstrated the feasibility of a "pump-probe" optical detection method for standoff sensing of chemicals on surfaces. Such a measurement uses two optical pulses – one to remove the analyte (or a fragment of it) from the surface and the second to sense the removed material. As a particular example, this project targeted photofragmentation laser-induced fluorescence (PF-LIF) to detect of surface deposits of low-volatility chemical warfare agents (LVAs). Feasibility was demonstrated for four agent surrogates on eight realistic surfaces. Its sensitivity was established for measurements on concrete and aluminum. Extrapolations were made to demonstrate relevance to the needs of outside users. Several aspects of the surface PF-LIF physical mechanism were investigated and compared to that of vapor-phase measurements. The use of PF-LIF as a rapid screening tool to "cue" more specific sensors was recommended. Its sensitivity was compared to that of Raman spectroscopy, which is both a potential "confirmer" of PF-LIF "hits" and is also a competing screening technology.

ACKNOWLEDGEMENTS

TABLE OF CONTENTS

1. INTRODUCTION

This report summarizes the results of an LDRD-funded effort to develop an optical detection method to allow stand-off sensing of chemicals on surfaces. As a particular example, it targeted the detection of surface deposits of low-volatility organophosphonate (OP) chemical warfare agents (to be referred to as LVAs). The remote characterization of chemical residues on a substrate is a problem for which only limited tools currently exist. It is, nevertheless, an area of fundamental importance to homeland and military defense because many threat and indicator materials exhibit low volatility and are likely to be found as a molecular or particulate surface deposition. Examples include LVAs, biological organisms and toxins, nuclear particulates, and explosives. Traditional optical remote sensing methods based on light absorption often fail in sensing trace surface deposits because their spectral signatures are masked by that of the underlying material. Methods based on fluorescence may not succeed for that reason or because the analyte does not fluoresce efficiently. As an alternative, we have explored the use of pulse-probe measurements that apply two pulses of light to the surface – one to remove the analyte (or a fragment of it) from the surface and the second to sense the removed material. This extends similar measurements [xv,xiii] that have been conducted in the vapor phase to the solid phase. For the selected case of LVA detection, the first pulse photofragments the nonfluorescent agent to release the highly-fluorescent phosphorous oxide (PO) radical as a vapor, and the second pulse detects the PO using laser-induced fluorescence (LIF). Thus, the first pulse serves the dual purpose of removing the analyte fragment from the surface and converting an undetectable analyte into a detectable (fluorescent) byproduct. The method is referred to as photofragment laser-induced-fluorescence (PF-LIF).

The results of this effort have demonstrated that PF-LIF is a viable method for sensing LVAs on common surfaces. They show that all four LVA surrogate species that were tested can be detected on all of eight realistic (concrete, aluminum, painted steel, wood, paper, oxidized steel, tar and plastic) for which tests were conducted. It was observed that the deep UV (200-250 nm) is a particularly useful spectral region for exciting LIF on surfaces because appears to stimulate relatively low background LIF from common materials. The detection limit for single-pulse-pair measurements (i.e., one PF pulse, one LIF pulse) was established and was found to be consistent with the needs of outside users. The pulse energies required for the measurement appear to be attainable by the use of commercial solid state pump lasers that can operate at high repetition rate (~1 kHz), thus allowing very rapid measurement or scanning.

At this point, the best use of PF-LIF for LVA detection appears to be as a trigger to quickly find deposits of LVA materials. Once found, the detection would be substantiated by a more selective detector, such as a mass spectrometer. This separation of roles is motivated by the fact that PF-LIF is very fast and capable of scanning a surface from a standoff distance. It is, however, subject to false alarms caused by benign phosphate-containing materials, as was proven by the generation of positive signal from a phosphate-containing detergent.

Raman spectroscopy was tested as a possible alternative to a mass spectrometer (or other point sensor) for substantiating PF-LIF "hits". Its use is attractive because both PF-LIF and Raman can be performed with the same instrumentation. This testing also served to guage

the relative performance of PF-LIF to Raman, which is a competing technology for standoff searching. It was shown that Raman can produce spectra that are detailed enough to allow discrimination between three different LVA simulants and the phosphate detergent that produced the false alarm. However, it was also shown that Raman is substantially (~3000X) less sensitive than PF-LIF when measured under the conditions tested. A particular limitation was found to be the interference from ablative processes that occur when the laser energy is increased in order to increase the Raman signal. This could be alleviated, to some degree, by increasing the area illuminated on the surface, or by increasing the pulse duration of the laser (perhaps to the extent that continuous-wave excitation is used). Both would reduce the intensity of the beam and avoid ablation. The degree to which this would improve the Raman measurement remains to be determined and is beyond the scope of this study.

The study revealed certain issues that arise when translating a vapor-phase pulse-probe method to the condensed phase. The high intensity of light required to fragment molecules in the vapor phase is beyond the ablation threshold for many common surfaces. Thus, the PF-LIF measurements of LVAs on surfaces were accompanied by the formation of a plasma. This posed new sources of background radiation (from broadband and narrow thermal plasma emission) and physical-chemical processes that affect the state of the analyte. With regard to the latter, a particular question that arose was whether the measured PO originated from fragmentation of the analyte or from recombination of P and O that were generated when the analyte was atomized by the plasma. Experiments showed that, shortly after the PF pulse, there was relatively little detectable PO and some detectable P. Thus, a recombinative mechanism appears to occur; however, the extent of its contribution is unclear at this time. Other differences observed had to do with the relative importance of reactive channels that remove PO and with the optimal PF-probe delay at which to measure the PO.

The LDRD lab measurements were closely coupled with discussion with potential customers and collaborators at outside organizations. These included customers at the Department of Homeland Security (DHS) and the Defense Threat Reduction Agency (DTRA). It also involved possible collaborators at the Edgewood Chemical Biological Center (ECBC). These contacts are continuing beyond the duration of this project.

2. BACKGROUND

2.1 Past PF-LIF measurements

Many polyatomic molecules pose a challenge to direct spectroscopic stand-off detection due to weak optical transitions and/or broad spectral features. For some such species, photofragmentation-fragment detection (PF-FD) approaches have been developed, in which a laser photofragments the target molecule and yields a daughter species that can be detected by subsequent absorption or emission [i]. PF/FD has been demonstrated for short-range stand-off detection of several species, including metal-containing compounds [ii,iii,iv,v,vi,vii,viii], nitro-containing energetic materials [ix,x,xi,xii,xiii,xiv], and organo-phosphonate chemical agent surrogates [xiii,xv,xvi]. Quantitative evaluations of PF/FD methods are generally limited to the vapor-phase. When applied to liquids and solids, quantifying PF/FD methods is complicated by the potential creation of surface plasmas: not only will the emission from the plasma interfere with the detection of the daughter species, but the plasma itself can alter the pathway through which the daughter species is generated. There is one notable exception to this, and that is the detection of condensed-phase nitro-containing explosives on surfaces [xvii]. For these molecules, the bond energies are sufficiently low that a single UV photon can drive the necessary dissociation processes, and the UV absorption cross sections are relatively high as well, allowing for efficient photodissociation at pulse energies well below the plasma-creation threshold. Unfortunately the situation is not so favorable for organophosphonate molecules. Therefore, to gain an understanding of the signal formation over a range of expected sensing scenarios, we have evaluated the temporally varying, spatially and spectrally dependent probe-induced emission while varying such parameters as the concentration of the parent species, the pump and probe pulse energies, and the deposition surface material.

2.2 Fluorescence detection of PO

The detection of PO radical by LIF has been described in the past by Wong [xviii]. The LIF process measures photons emitted by PO after excitation of an electronic state of the radical. The known electronic states of PO are described in Figure 1. Those for which LIF-active transitions have been published are defined in color. The ground state ($X^2\Pi_r$) is shown in green and the two excited states from which LIF has been observed are indicated in red ($A^2\Sigma^+$) and blue ($B^2\Sigma^+$). According to Wong, A is a Rydberg state, which would cause the A$\rightarrow$X transition to exhibit a higher intensity than the non-Rydberg B$\rightarrow$X transition. Perhaps for this reason, the past PF-LIF measurements of Long [xv] and Shu [xiii] detected PO via the A$\rightarrow$X transition; this is the pathway selected for use in this project as well. Operation at the shorter emission wavelength (247 nm vs. 327 nm) of the A$\rightarrow$X transition also has the advantage of low solar background (the region below 300 nm is considered "solar blind"), and low LIF background when contaminants are measured on many common materials [xix]. Conversely, an avantage of the longer wavelength is that it is easier to generate 327 nm laser radiation than 247 nm, so 327 nm might be considered more appropriate for a fieldable system.

The PO A-X excitation-emission process used in this project is described in Figure 2. At far left is a diagram showing the X$\rightarrow$A transition, which is caused by the 246.3-nm probe laser pulse. Each X vibronic state (labeled by its v quantum number) is split into two spin levels

separated by 224 cm^{-1} (spin = 1/2, 3/2) by spin-orbit coupling. This leads to two absorption band systems, one having a Q-branch peak at 246.25 nm and the other peaking at 247.62 nm. The longer-wavelength band was used in this project, although the shorter-wavelength band should actually produce a somewhat stronger signal [xiii]. Excitation of both bands was tested by us and produced similar results; however, it is possible that one or both of the measurements were saturated at that time.
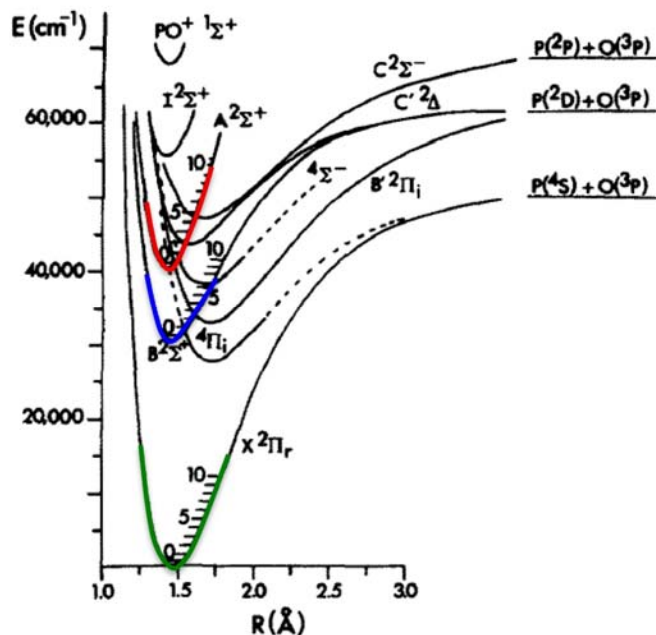
Figure 1 – Diagram of the electronic states of the PO radical (duplicated from [xviii]).

Once excited, the PO A state emits to both the X state (at wavelength near 255 nm) and the B state (at wavelengths near 1000 nm), as show in Figure 2. The ratio of emission rates (Einstein A coefficients) for these two transitions is A_{AB}/A_{AX} = 0.12, according to Wong. Thus, it seems reasonable to ignore the A→B emission, as is being done in this project.

As shown in the right-most panel of Figure 2, the A→X emissions occur from the v=0 level of the A state to the two spin sub-levels of the v=1 and the v=2 vibrational levels of the X ground state, causing a pair of split peaks in the fluorescence spectrum (rightmost panel of Figure 2). The radiative lifetime of this emission was reported to be 9.68 ± 0.47 ns [xviii].

As the PO A state is radiating, its population is also being lost to quenching. The effect of quenching at atmospheric pressure has been evaluated by Shu using the radiative lifetime of the state and quenching coefficients (1.8 x 10^{-10} cm^{3}molecule^{-1}s^{-1} for O_2 and for N_2) measured by Long and Sausa. They determined the fluorescence quantum yield of the state in the presence of quenching to be 0.19 at 100 torr of air and 0.03 at atmospheric pressure of air. Later in this report, we compare the relative fluorescence signals of PO →X emission at several pressures of air.
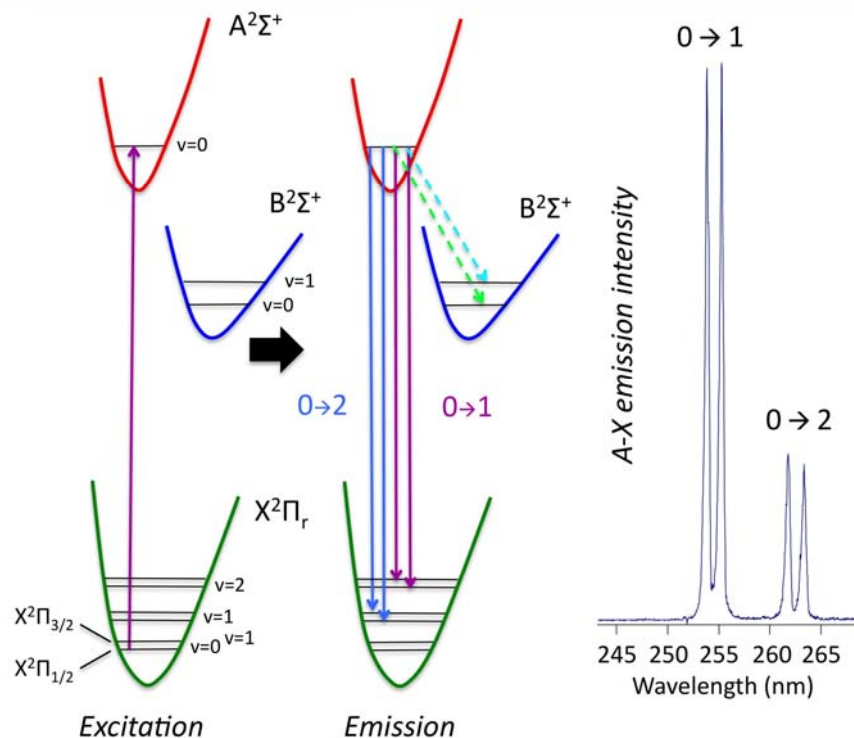
Figure 2 – Diagram of the excitation-emission process of the A→X transition (left) and assignment of the LIF emission spectrum of the PO radical.

A reactive channel also exists that removes ground (X) state PO molecules by reaction with O_2 to form PO_2. The rate of the reaction was reported [xx] as 1.4×10^{11} cm^{3}molecule^{-1}s^{-1}, which implies a radical lifetime of 13 ns in the presence of an atmospheric oxygen concentration. Because the reactive state is X, this does not affect the LIF yield of the A state. It does, however, represent a significant loss of PO population that can occur during the time between the PF pulse and the probe pulse. As will be seen, we saw behavior that was inconsistent with such a fast reaction rate; however, this may have been caused by the production of a plasma by the PF pulse on the solid surface.

2.3 Processes affecting PF-LIF detection of OP's on surfaces

Figure 3 summarizes the dominant processes that can affect the detection of OP agents on surfaces using PF-LIF. It shows that the analyte on the surface can undergo fragmentation to produce PO radical. Alternatively (or in parallel), if the energy exceeds the ablation threshold of the surface, a plasma can form which could atomize the analyte and a portion of the surface as well. Phosphorous and oxygen atoms generated in the plasma can reform PO; depending on conditions – none, some, or all of the detected PO may be produced through this channel. The PO signal is created by A→X LIF in the presence of the competing processes described in the previous section (oxygen reaction to PO_2, competition with A→B emission, quenching). Background signals are potentially generated by probe-laser-induced fluorescence, Raman scattering from the surface, and residual plasma emission (if any) that exists at the delay time at which the measurement is made after the initial PF pulse.
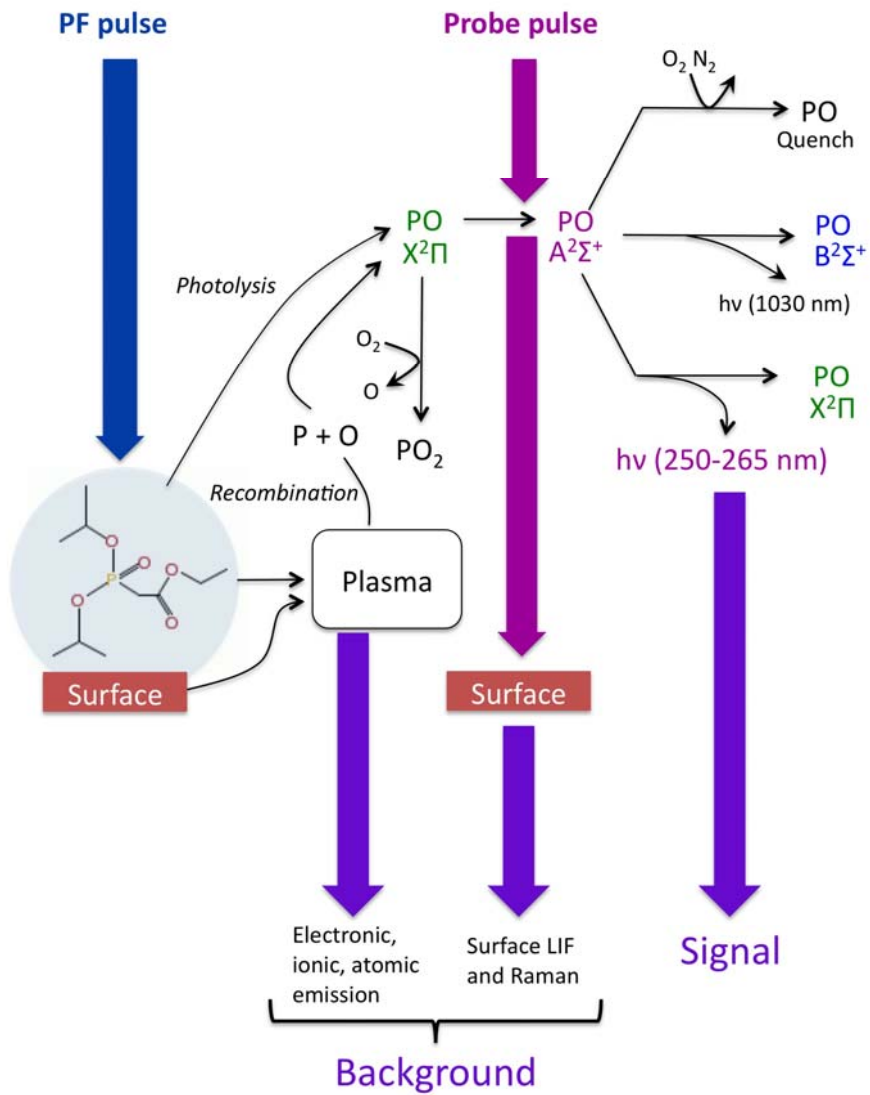
Figure 3 – Processes affecting the detection of OP agents using PF-LIF.

3. SEQUENCE OF THE FEASIBILITY AND PERFORMANCE ASSESSMENT

The measurements made during this project proceeded in steps that increasingly challenged the feasibility of the method and quantified aspects of its performance. The steps that were carried out are:

1. Assembly of a versatile laboratory apparatus
   A laser apparatus was assembled that allows PF-LIF measurements on both gas-phase and condensed-phase samples. The system consists of a frequency quadrupled Nd:YAG laser to provide the PF pulse and a nonlinearly upconverted dye laser to provide LIF-excitation pulses. Detection is accomplished using an intensified-CCD-based spectrometer. The system is versatile in allowing broad adjustment of laser intensity on the sample, LIF excitation wavelength, relative timing of the laser pulses, and spectrometer detection conditions (gain, gate-width and timing, and signal integration).

2. Reproduction of prior gas-phase PF-LIF measurements
   Gas phase PF-LIF measurements were reproduced under conditions similar to those published by Long [xv] and Shu [xiii]. This allowed us to establish familiarity with the reaction conditions and to test the apparatus.

3. "Quick and dirty" assessment of PF-LIF detection on a surface
   The gas-phase measurements were extended, for the first time, to measurement on a surface. This was accomplished by measuring DMMP that was deposited without quantification on an aluminum substrate. The measurement represented a go/no-go point in the project. From this point on, all of our studies focused on surface-deposited materials.

4. Determination of a simulant that is representative of LVAs
   A survey of potential simulant materials [xxi] was conducted in order to identify one that represents the properties (i.e., boiling point, vapor pressure, presence of an organophosphonate group) of a nominal LVA (VX), but which was not too toxic to handle.

5. Evaluation of the generality of the method
   The extension of the method to the measurement of other simulants (DEMP, DIMP, DIPP) on other surfaces (concrete, wood, plastic, paper, oxidized steel) was tested.

6. Development of a method to quantitatively deposit simulants on surfaces
   An airbrush method was developed and tested to control the amount and spatial distribution of simulant deposited on the surface during sensitivity analyses.

7. Development of performance metrics
   Metrics were developed to judge the performance of the method against the needs of potential customers. One was based on prior requirements stated by the Department of Homeland Security (DHS); the other was based on the sensitivity requirement for clearance of a facility from VX contamination (as specified by the U.S. Environmental Protection Agency (EPA)).

8. Measurement of the sensitivity of the method
   Two surfaces were identified for more detailed measurement – aluminum and concrete. They were selected because their porosities and thermal conductivities vary greatly from each other. Porosity affects the diffusion of simulant into the substrate. Thermal conductivity affects the manner in which the substrate dissapates the ablative laser radiation.

9. Enhancement of the sensitivity of the method by adjusting laser pulse conditions
   The dependence of chemical detection sensitivity on the delay time between the PF and LIF pulses, and on their energies was tested. A premium was placed on minimizing the energy per pulse to allow implementation of a compact and high repetition-rate system, which would increase scanning speed.

10. Determination of optimal focusing of the probe laser pulse
    Planar laser-induced fluorescence (PLIF) measurements were made to image the spatial extent of the plume after ablation. This was used to optimally match the size of the focused probe beam to the plume, which is a requirement to achieve optimal sensitivity and efficiency.

11. Investigation of the PO formation mechanism
    Our recognition that other have observed that LIBS can produce diatomic species (such as PO) through the recombination of atomic species led us to wonder whether the PO that we were observing was formed in a similar way. This suspicion was was heightened by the fact that maximum signal was collected at a relatively long delay between the PF and LIF pulses, which would be consistent with an significant recombinative pathway. Experiments showed that recombination could be occurring; however, its extent is still undetermined.

12. Evaluation of interferences
    Because PO is a relatively non-specific indicator of OP presence, other phosphate-containing materials were tested for response to PF-LIF. Phosphate soaps were found to generate a signal.

13. Evaluation of Raman spectroscopy as an orthogonal measurement
    In order to address the relatively low specificity of the PF-LIF method, the potential of using Raman spectroscopy as a confirmatory channel was investigated. The Raman measurement can be made with the same instrumentation used to perform PF-LIF. A combined system would be used in a staged fashion, in which PF-LIF would serve as a rapid scanning device to isolate areas of high phosphonate concentration, and Raman would be used to confirm that the "hit" is caused by OP chemical agents.

14. More uniform sample generation
    A method was identified and implemented that generates more uniform coverage of liquid simulants on substrates. The method employs an inkject printer head to deposit droplets of known diameter on a surface at specified surface coverage.

15. Prescription of a fieldable system
    Based on the performance of the laboratory system and on consideration of available hardware (lasers, detectors) that are useable for field operation, the design of a fieldable system that could be implemented by an outside customer was prescribed.

4. INSTRUMENTAL APPARATUS AND SAMPLE PREPARATION

The apparatus used to conduct the PF-LIF and Raman experiments is a flexible laboratory system that allowed the behavior of PF-LIF and Raman measurements to be evaluated under a wide variety of experimental conditions. It was not intended to be a fieldable instrument. The apparatus was used make two types of measurements – spectroscopic and imaging. The configurations used for each are described in the following sections.

4.1 Spectroscopic configuration and initial vapor-phase measurements

The proof of feasibility began with measurements in the vapor phase that replicated previously published experiments. Figure 4 contains a diagram of the gas cell, which is constructed from stainless steel vacuum hardware. The cell is capable of being evacuated and filled by either static or flowing gas mixtures containing DMMP. The cell is heated by thermal tape to prevent vapor condensation. DMMP vapor is created in a bubbler that is connected to the cell by stainless-steel tubing, and which is heated to approximately 40 degrees C to evaporate the chemical.
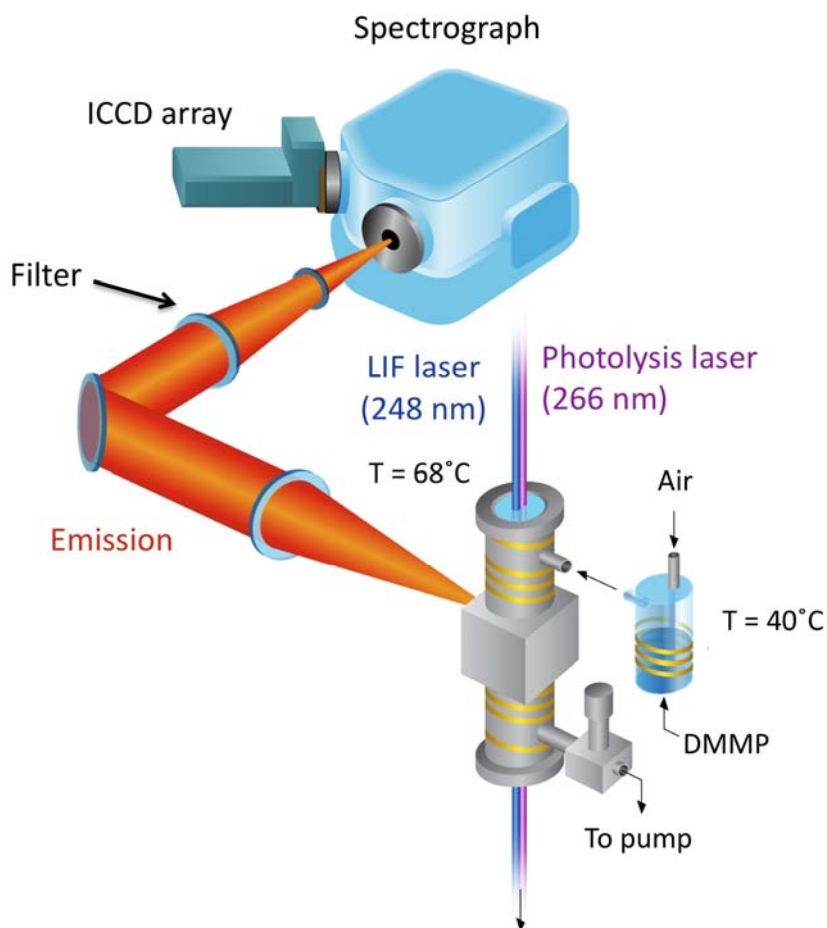

Figure 4– Diagram of the gas-phase measurement apparatus.

Laser radiation passes through the cell via wedged fused-silica windows mounted at its top and bottom ends. The PF pulses used in all experiments (vapor and solid) were created

using a frequency-quadrupled Nd:YAG laser emitting 7-ns pulses at 266-nm wavelength. It was used to produce pulse energies in the range between 70 and 3000 μJ, depending on the experiment. The PF pulse was focused to a spot (or waist, for the vapor measurements) having a diameter of about 70 μm and, thus, having an intensity ranging from approximately 250 MWcm^{-2} to 11 GWcm^{-2}, in the approximation of a square temporal pulse and a flat-top intensity profile. It should be pointed out, however, that the spatial profile of the ablation pulse was irregular, and the multi-mode output of the Nd:YAG laser caused mode-beating "spikes" in the temporal profile of its pulses. Thus, the quoted intensities are only to be considered average reference points.

Excitation of PO LIF was accomplished using a tunable probe laser pulse that was usually set to wavelength 248.5 nm, and which was created by mixing the pulsed output of a frequency-doubled, tunable dye laser with a Nd:YAG laser pulse (1064 nm). The probe pulse was set to have an energy somewhere in the range of 25-250 μJ, depending on the experiment. Its duration was ~7 ns and it was formatted to be colinear with the ablation pulse and to focus to a diameter of ~80 μm at the sample. The pulse was triggered to occur at at delay of 0-3000 ns after the PF pulse, depending on the experiment.

As depicted in Figure 5, the PF-LIF event occurs at the common focal position of the overlapped pulses, which is located in the center of the vapor cell for the gas-phase experiments. Fluorescence signal was collected through a window mounted in the side of the cell (obscured at the left of the cell in Figure 4), by a pair of lenses (50-mm diameter; 300-mm focal length) that imaged the optical signal onto the entrance slit of a grating spectrograph. The spectrograph was a Czerny-Turner type (McPherson Inc., Chelmsford, MA; Model 218) that accepted light at f/5.3. Thus, its acceptance solid angle was slightly underfilled by that of the input light (f/6). Its entrance slit was oriented parallel to the laser beam axis and was adjusted to a width (typically 200 μm) that is sufficiently wide to span most of the radiating sample image while maintaining acceptable spectral resolution. For the gas-phase measurements, the radiating zone was a vertically oriented, cylindrical volume (Figure 5) that was projected as two-dimensional image in the slit plane. It was defined by the overlap of the LIF excitation laser with the cylindrical region of PO radical produced by the PF pulse. For condensed-phase measurements, the emitting region was the excited portion of the plume that was produced by surface photofragmentation, as described in the next section.

Once dispersed, the optical signal was imaged by the spectrograph onto the photocathode of an intensified charge-coupled devise (ICCD) array detector (Andor Model DH501i-25F-04) having 1024 x 128 pixels. Spectroscopic measurements were conducted by on-chip binning of the array pixels in the vertical dimension to create a linear, 1024-element-long spectrum. The photocathode has a near-uniform quantum efficiency of about 13-15% over the wavelength range of 200-300 nm (encompassing all signals measured in this project). The intensifier was gated to amplify photoelectron signals at gains of up to 400X for gate widths (usually ~20 ns) that were large enough to integrate the short lived (~3 ns lifetime at atmospheric pressure) PO LIF in the presence of temporal jitter in the LIF excitation pulse; but were short enough to maximally reject thermal-plasma or elemental emission produced by the fragmentation pulse. Similar gating conditions were used to collect the instantaneous Raman scattering.

VAPOR-PHASE EXPERIMENTS

1. Fragmentation pulse   2. Fragment plume   3. LIF excitation

SURFACE EXPERIMENTS

1. Fragmentation pulse   2. Fragment plume

3A. LIF excitation

3B. PLIF excitation
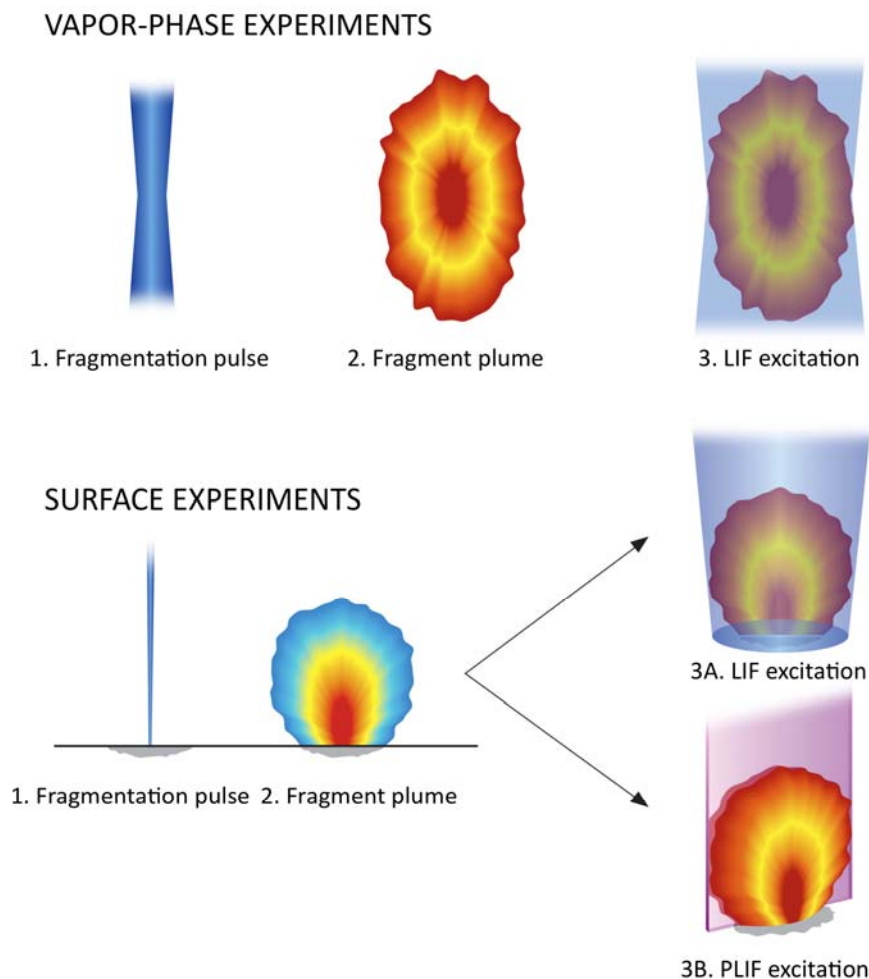
Figure 5 – Depiction of the vapor-phase PF-LIF process (top row) and the surface PF-LIF processes (bottom row).

Rejection of scattered laser radiation from the PF or LIF/Raman excitation pulses was accomplished using temporal and spectral filtering. Most photons from the PF pulse were temporally rejected because signal was collected at a relatively long (≥20 ns) delay after its firing. Any residual PF scatter was separated from the signal by dispersion in the spectrograph. Rejection of the 248-nm LIF-excitation pulse required additional spectral filtering, since it could not be temporally removed when exciting the short-lived (<3-ns lifetime) PO LIF (or the instantaneous Raman signal). That was accomplished using a rejection filter (Barr Associates, 4.6-nm width, 31% peak transmission, >10^4 out-of-band rejection), as shown in Figure 4.

4.2 Spectroscopic configuration for PF-LIF and Raman on surfaces

The apparatus used to test spectroscopic PF-LIF detection on surfaces is shown in Figure 6. Here the sample consisted of a disk that is composed of a specific matrix material (e.g. aluminum) and is coated with LVA simulant. These experiments used the same laser and spectrometer systems as were used for the gas-phase experiments. The laser pulses were also focused similarly to the gas-phase conditions unless the effects of focusing were being

tested. This typically produced a PF-laser spot size ($1/e^2$ intensity radius) of 23 x 40 μm on the surface, and an LIF-excitation spot size of 70 x 51 μm.
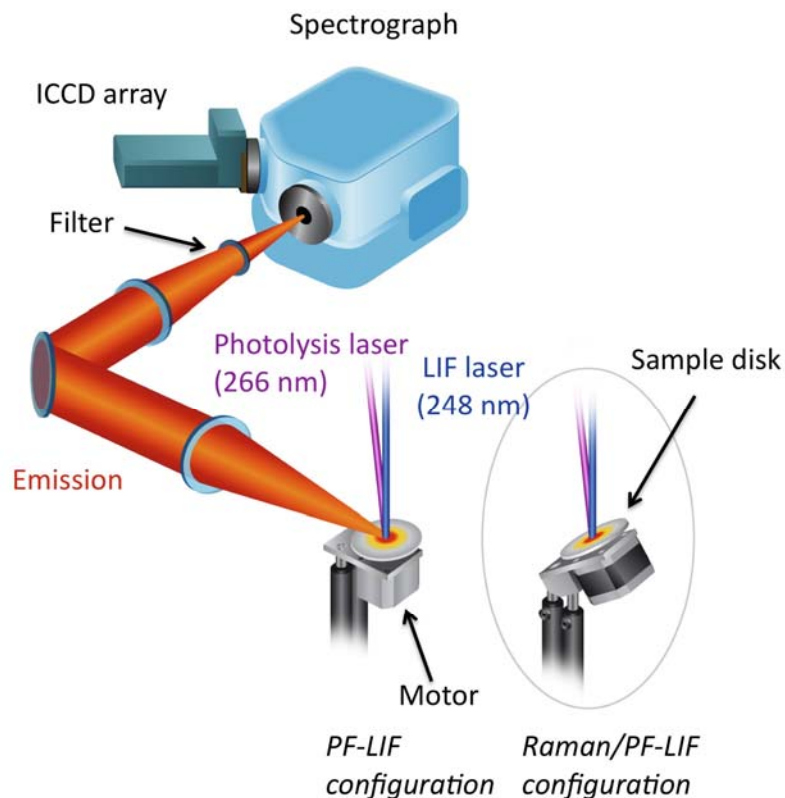
Figure 6 – Diagram of the surface PF-LIF apparatus.

In measuring trace coatings of materials on surfaces with a PF step, the possibility of depleting the simulant layer arises. To mitigate the this effect, the sample was mounted on a motor axle and rotated so that a fresh portion of the surface was underneath the interrogation region for each pulse pair. This also served to average over inhomogeneities in the amount of deposited analyte.

Most PF-LIF measurements were made with the lasers normally incident on the sample (left sample diagram in Figure 6).   An illustration of the sequence of measurement events that occurred on the sample is shown in the bottom row of Figure 5. The initial (PF) laser pulse (left panel) impinged on the sample to generate the fragmentation plume (center panel). After a prescribed time delay, the second (LIF) laser pulse illuminated a portion of the plume (upper right panel) to excite PO LIF. An alternate configuration illuminated the plume with a sheet of laser light (lower right panel) to cause planar laser-induced fluorescence (PLIF). Those experiments are described in the next section.

The spatial overlap of the LIF-excitation pulse with the ablation plume (upper right panel of Figure 5) produces a (approximately cylindrical) volume that radiated PO fluorescence. This was imaged on the slit plane of the spectrograph. Clearly, more signal will be generated if the excitation laser diameter effectively overlaps the plume, and if the spectrometer slits encompass most of the plume image. This was tested during the PLIF experiments described in the next section.

Experiments to measure surface Raman scattering could not use the normal-incidence-laser geometry because the Raman signal would be produced in the plane of the surface and this would not be viewed by the spectrograph. Instead, the sample was tilted so that its normal formed a 45-degree angle with the laser-incidence and spectrometer-collection axes. In this case, the PF-pulse intensity on the target would be reduced by about cos(45) and the plume would be elongated in the vertical direction (as viewed by the spectrograph).

When Raman measurements were made, only the 248-nm pulse was used. Because the intensity of collected Raman scattering was polarization dependent, it was necessary to properly orient the polarization of the 248-nm pulse. A ½-wave plate was used to set the polarization so that it was oriented 90 degrees from the collection axis and parallel to the sample plane.

4.3 Imaging configuration

Optimal excitation of the ablation plume motivated imaging experiments (see Figure 7) that would directly observe its formation and evolution. These were accomplished by illuminating the plume with sheet of light produced from the 248-nm pulse using a cylindrical lens (lower right diagram in the bottom row of Figure 5). The resulting plane of PO LIF was imaged directly onto the photocathode of the ICCD array after passing through a bandpass filter that transmitted wavelengths between XX and XX nm.
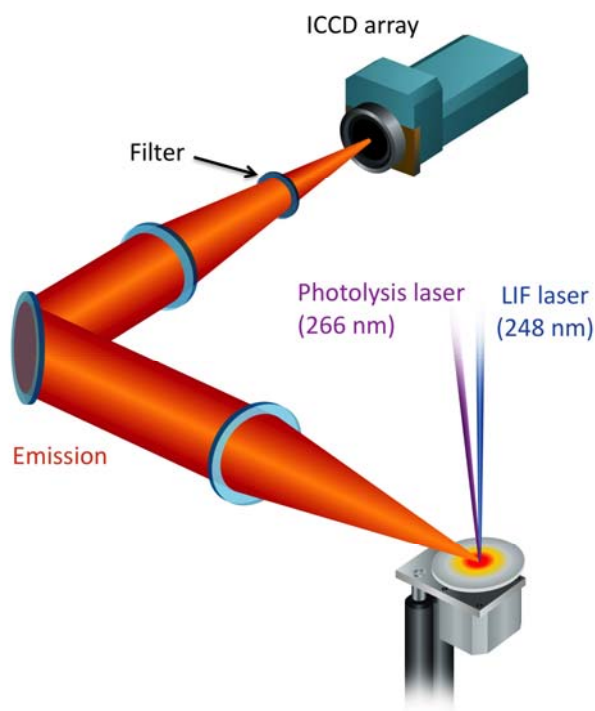

Figure 7 – Diagram of the PLIF experimental configuration.

4.4 Simulant materials

The molecular structures of the organophosphonate nerve agent simulants that were used in this project are illustrated in Figure 8. Their physical properties are listed in Table 1. All

four are alkyl esters of phosphonic acid (R'PO(OR")$_2$. Three (dimethyl methyl phosphonate – DMMP; diethyl methyl phosphonate – DEMP, and diisopropyl methyl phosphonate – DIMP) are accepted nerve agent simulants in which R'=CH$_3$ and the R"s are progressively larger alkyl groups (CH$_3$, CH$_2$CH$_3$, CH$_2$(CH$_3$)$_2$). Initial measurements were made with DMMP and DEMP to replicate past experiments. Subsequent measurements were conducted with DIMP and diisopropyl isopropyl phosphonate (DIPP) in an effort to assess the detection method on a lower vapor-pressure simulant. Ultimately DIPP was selected as the simulant to be used in the remainder of the project because it has the lowest vapor pressure of all four.
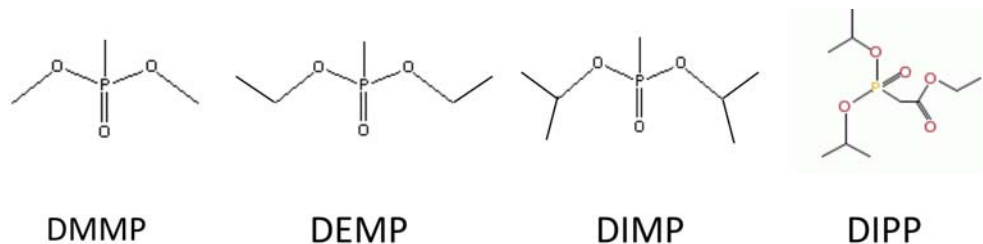
Figure 8 – Molecular structures of the organophosphonate nerve agent simulants used in this project.

Table 1 – Properties of CWA simulants used in this project

Material	Molecular weight (g)	Vapor pressure (torr @ T Kelvin)	Boiling point (°C)
DMMP [xxii]	124	0.59 @ 293	181
DEMP [xxii]	152	0.28 @ 293	194
DIMP [xxii]	180	0.21 @ 293	121[a]
DIPP [xxiii]	252	Uncharacterized	142-143[b]

  a. At 10 mm Hg reduced pressure
  b. At 11 mm Hg reduced pressure

4.5 Deposition methods

4.5.1 Deposition apparatus based on the use of an airbrush

The DIPP simulant was deposited on various surfaces using the apparatus shown in Figure 9. It employed a commercial airbrush that was loaded with the liquid simulant and which sprayed it through an aperture and onto the selected matrix. The deposition density was controlled by a mechanical shutter that rotated to block or unblock the aperture for a prescribed amount of time, thus regulating the spray duration. The shutter motion (and the exposure time) were controlled by digital commands from a computer program. The matrix sample was weighed before and after deposition to verify the mass of material that was deposited.

While convenient, the airbrush produced a surface deposition that was not uniform over the sample surface. This was mitigated, to some degree, by rotating the sample as a measurement was being made, using the motorized sample holder shown in Figure 6. Section XX displays a spatially resolved PF-LIF measurement of the surface sample density.
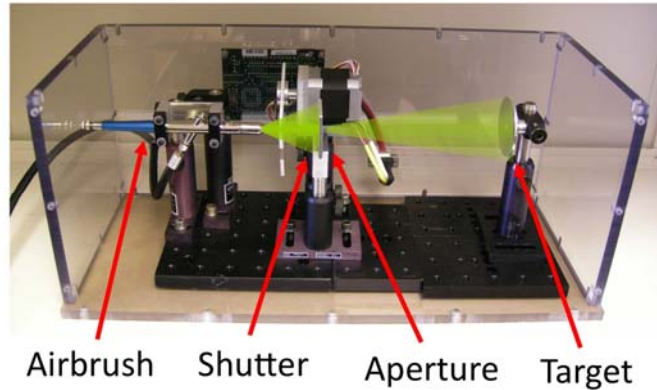
Figure 9 – Photograph of the simulant deposition apparatus used in this project.

4.5.2 Deposition apparatus based on the use of an inkjet printer head

In the last year of the project, a droplet generator was purchased from Microfab Technologies (Plano, TX), which was used to create samples with a more uniform surface coverage than produced by the airbrush. The Microfab system uses a piezoelectric-driven inkjet printing head to produce individual droplets (see Figure 10) of highly repeatable size at a wide range of repetition rates. The print head that was received was equipped with a 60-μm-diameter aperture to make droplets that were slightly less than 60 μm in diameter when the DIPP simulant was being dispensed. The print head was mounted above a pair of orthogonal motor-driven stages that were programmed to move the sample surface underneath the droplet deposition area in a raster pattern. The dimensions of the raster and the droplet release frequency were adjusted to create the desired coverage of simulant on the sample. The system was calibrated for droplet mass by depositing a known number of droplets and comparing the substrate weight before and after deposition.

Figure 10 – Photograph of a droplet falling to the surface after generation by the inkjet.

Figure 11 – Photograph of the inkjet apparatus used to coat substrates.

5. RESULTS

5.1 Gas phase measurements

Vapor-phase DMMP was successfully measured using PF-LIF in the apparatus of Figure 4. Spectra collected as a function of buffer gas press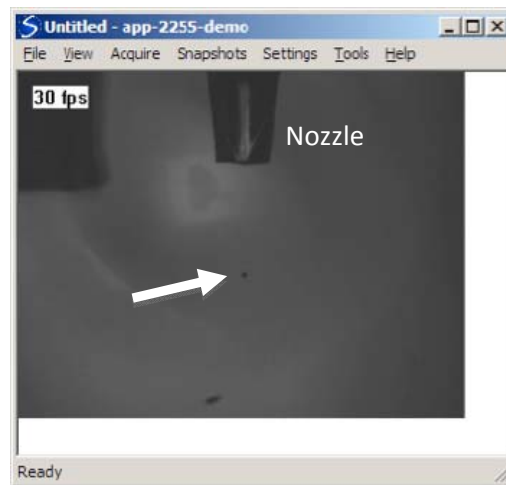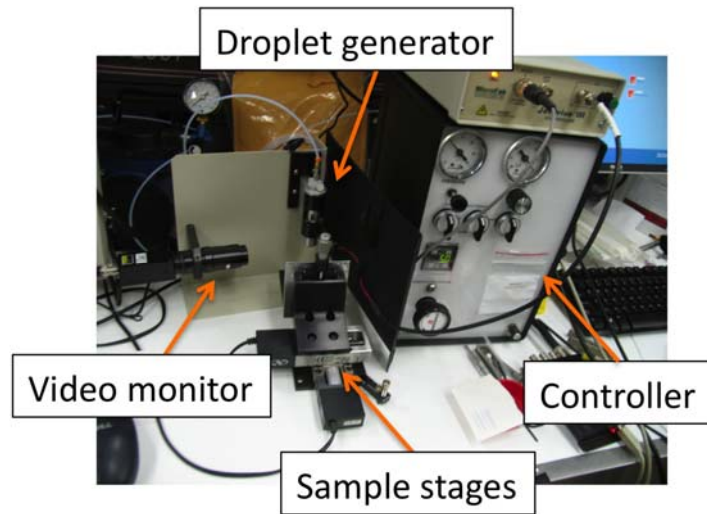ure are shown in Figure 12. As expected, they exhibit the split emission peaks of the PO A→X vibronic transitions (0→1, 0→2). They were obtained using samples of DMMP at a partial pressure of 2.3 torr (saturated vapor pressure at 313.2 K acccording to Butrow [xxii]) mixed with air to produce the indicated total pressures. The data demonstrate that a reduction in signal of about 3.3X occurs due to air quenching as total pressure changes from about 95 torr to near-atmospheric pressure. This extends the pressure range of DMMP PF-LIF measurements beyond those reported by Long (0.8 torr pure DMMP) and Shu (1 torr DMMP diluted to 100 torr in air). The observed reduction is not as great as the 6.3X reduction extrapolated by Shu using the radiative lifetime and measured N_2/O_2 quenching coefficients. The data demonstrate that, although air quenching reduces the PO signal, the signal remains useful at atmospheric pressure.
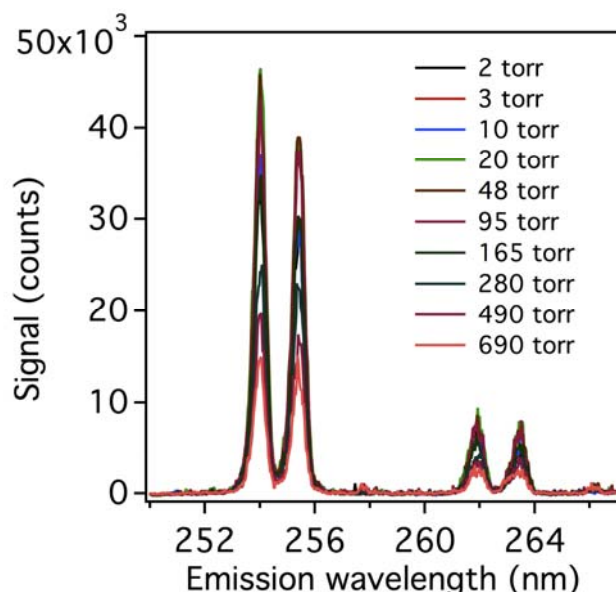
Figure 12 – Spectrum of PO LIF signal generated by gas-phase PF-LIF measurements using the apparatus of Figure 4. Spectra are plotted as a function of total pressure in the cell.

The power dependence of the photofragmentation process was also characterized and the results are shown in Figure 13. This was measured as nitrogen was bubbled through liquid DMMP held at a 40℃ (producing a vapor pressure of about 2 torr). The total cell pressure was 95.8 torr. The energy of the fragmentation beam was adjusted using a waveplate/polarizer combination and the integrated signal from both peaks of the the 0→1 transition was measured. The results demonstrate a slope of 2.09 when signal is plotted against photofragmentation energy in a log-log format. This is in good agreement with prior measurements [xv], which showed a slope of 2.2 for photolysis caused by a KrF laser and 1.9 for that caused by an ArF laser. As discussed by Long, this suggests a process that is dependent on at least two photons (or more, if additional steps are saturated).
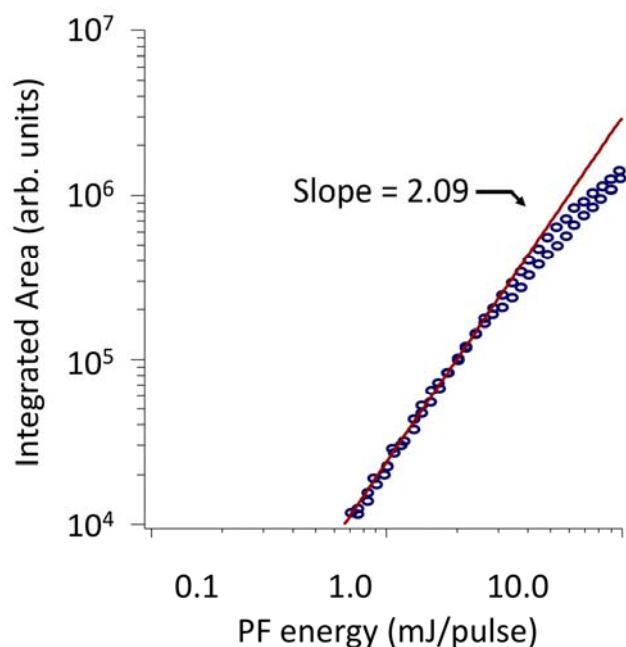
Figure 13 – Dependence of PO signal on the photofragmentation energy.

A test was conducted to determine the effect of temporal delay between the pulses on the signal. The results are shown in Figure 14 where the logarithm of the signal is plotted as a function of the delay between the PF and probe pulses. The signal shows a rapid rise in intensity as the delay is changed from 10 to 15 ns and a falloff after that. Because this project focused on the detection of condensed-phase OP materials, identifing the cause of this trend was not pursued. Sausa et al. observed an initial rise in signal, which they attributed to an increase in excitable PO lower-state population caused by collisional equilibration. They also saw a subsequent falloff that they attributed to the removal of PO by reaction with O_2 to form PO_2. Division of the slope of the linear region in Figure 14 by the rate constant for the $PO+O_2$ reaction (1.4 x 10^{-11} $cm^3molecule^{-1}s^{-1}$ [xx]) implies an oxygen partial pressure of 21.5 torr which is similar to that at which the experiment was conducted. The origin of the deviation from linearity of the 90 and 130 ns points is not known. Again, these measurements were made only to establish familiarity with the DMMP photolysis prior to the surface measurements, and were not meant to be a rigorous verification of the past data.

5.2 Beam profile and fluence measurements

It is important to consider the spatial distribution of the excitation beam energy when a nonlinear process such as PF is being used. The beam profiles of the PF and probe lasers were measured with a detector array and the results are plotted in Figure 15. It is clear that the beam shapes are irregular, particularly in the case of the PF laser. A pixel weighting was devised to determine an effective beam area and fluence. The effective area was calculated using:

$$A_{\text{eff}} = \frac{A_{\text{pix}} \cdot \left(\sum s_{ij}\right)^2}{\sum s_{ij}^2}$$ [1]

where A_{pix} is the area of a pixel in the array and $S_{i,j}$ is the signal of the pixel at position i,j. Once determined, the effective area was used to calculate the diameter of a circle of the same area. The area was also used to calculate the optical fluence for each beam. At the time of collection of the energy-dependence measurement of Figure 13, the probe laser was found to have an effective diameter of 67 μm and the PF beam an effective diameter of 76 μm. The fluence of the probe laser was determined to be 2.85 J/cm² per shot (at a total pulse energy of 100 μJ), and that of the PF beam was 11.12 J/cm² per shot (at 500 μJ energy).
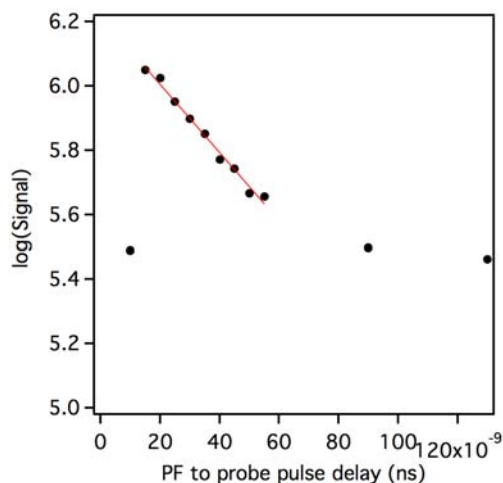
Figure 14 – Plot of the integrated signal from PF-LIF measurement of vapor phase DMMP as a function of the delay between the PF and LIF laser pulses.
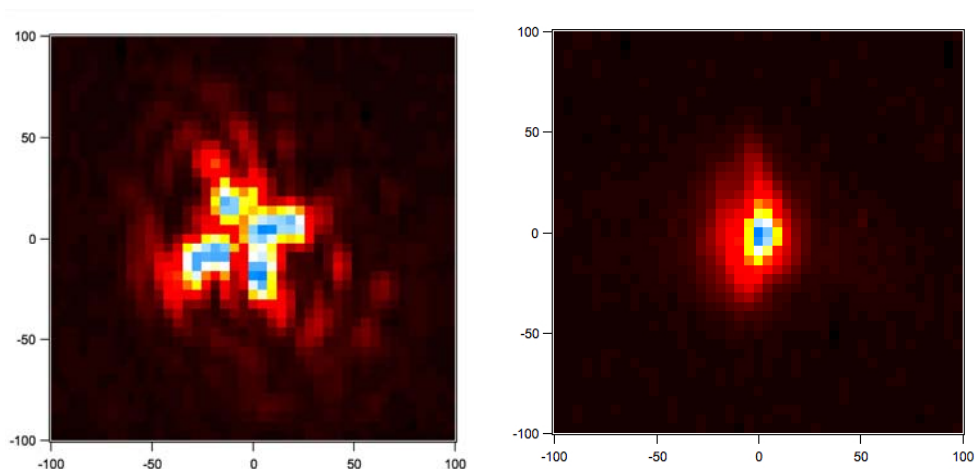
Figure 15 – Beam profile images of the 266-nm PF (left) and the 248-nm probe laser (right).

5.3 Surface measurements – generality of surface and simulant type

Following the vapor-phase measurements, attempts were immediately made to demonstrate PF-LIF of DMMP deposited on several realistic surfaces (concrete, painted metal, tar, paper, and oxidized steel). The results are shown in Figure 16. It is clear that the measurements were successful, and that no substrate LIF or Raman signals interfered with the strong PO-LIF signals produced by the relatively high concentrations (100's of μg cm⁻²)

24

of simulant used. The results suggest that the PF-LIF process has the potential to be useful on multiple surface types, and support the notion that there is a low LIF background when excitation occurs near 248 nm [xix].

In analogy to Figure 14, a series of measurements was also conducted to determine the dependence of the signal on the time delay between the PF and probe pulses. This is plotted in Figure 17. It is notable that the signal shows a monotonic increase with delay time. For this and most subsequent measurements made in this project, a delay time of 1 μs was found to be optimal. This is unlike the vapor phase measurements, where the signal decreased beyond a delay of 15-20 ns. The long increase in signal observed here is inconsistent with the existence of a $PO+O_2$ reaction, as it would be expected to remove PO at a rate faster than the decrease shown in Figure 14, given the higher (atmospheric) O_2 partial pressure.

Measurements were also made with multiple simulants to demonstrate that the reaction is not limited to fragmentation of a single molecular species. Figure 18 contains measurements made of the simulants DMMP, DIMP, and DIPP deposited on aluminum. The measurements were made under the conditions indicated in the panels. Similar results were obtained for DEMP on aluminum. In all cases, the delay between laser pulses was 1 μs and the ICCD gate width was 20 ns.

5.4 Quantitative surface PF-LIF and evidence of plasma formation

After the "go/no-go" measurements of the previous section, preparation for more careful and quantitative PF-LIF measurements of simulants on surfaces began. The apparatus of Figure 9 was assembled and used to deposit known amounts of DIPP simulant on disks of aluminum. In one case, a scanning procedure was used with the PF-LIF measurement to map the DIPP concentration distribution on the disk. As shown in Figure 19, the scanning method measured 200 points around the circumference of a series of circles of progressively larger radius on the disk. A single pair of laser pulses measured the DIPP PF-LIF at each of the 200 points, and there was no spatial overlap between adjacent measurements.

Before considering the mapped data, it is instructive to plot the signal integrated around each circumference as a function of radius. The spectrum in the center of Figure 19 shows an example of one such integration. In addition to the A→X vibronic lines, two additional features appear at 257.4 and 258.2 nm. These are attributed to the emission lines of aluminum atoms, which are apparently formed in an optical breakdown produced by the PF pulse on the surface. In addition to these emissions, evidence of breakdown was also observed in the form of a visible (and audible) spark on the surface. This is the same signal that would be produced in a laser-induced breakdown spectroscopy (LIBS) measurement of the sample for the same applied pulse energy, and these plasma-related signals will be referred to as LIBS signals in the remainder of this report. The audible and visible evidence of plasma were also observed during collection of the data in Figure 16 and Figure 18; however, no evidence of plasma emission was present on those data – probably because of the high concentratrion of simulant on those samples. The potential for optical breakdown represents a distinct difference between the vapor- and condensed-phase measurements, as the likelihood for breakdown is higher on a solid surface than in a vapor.
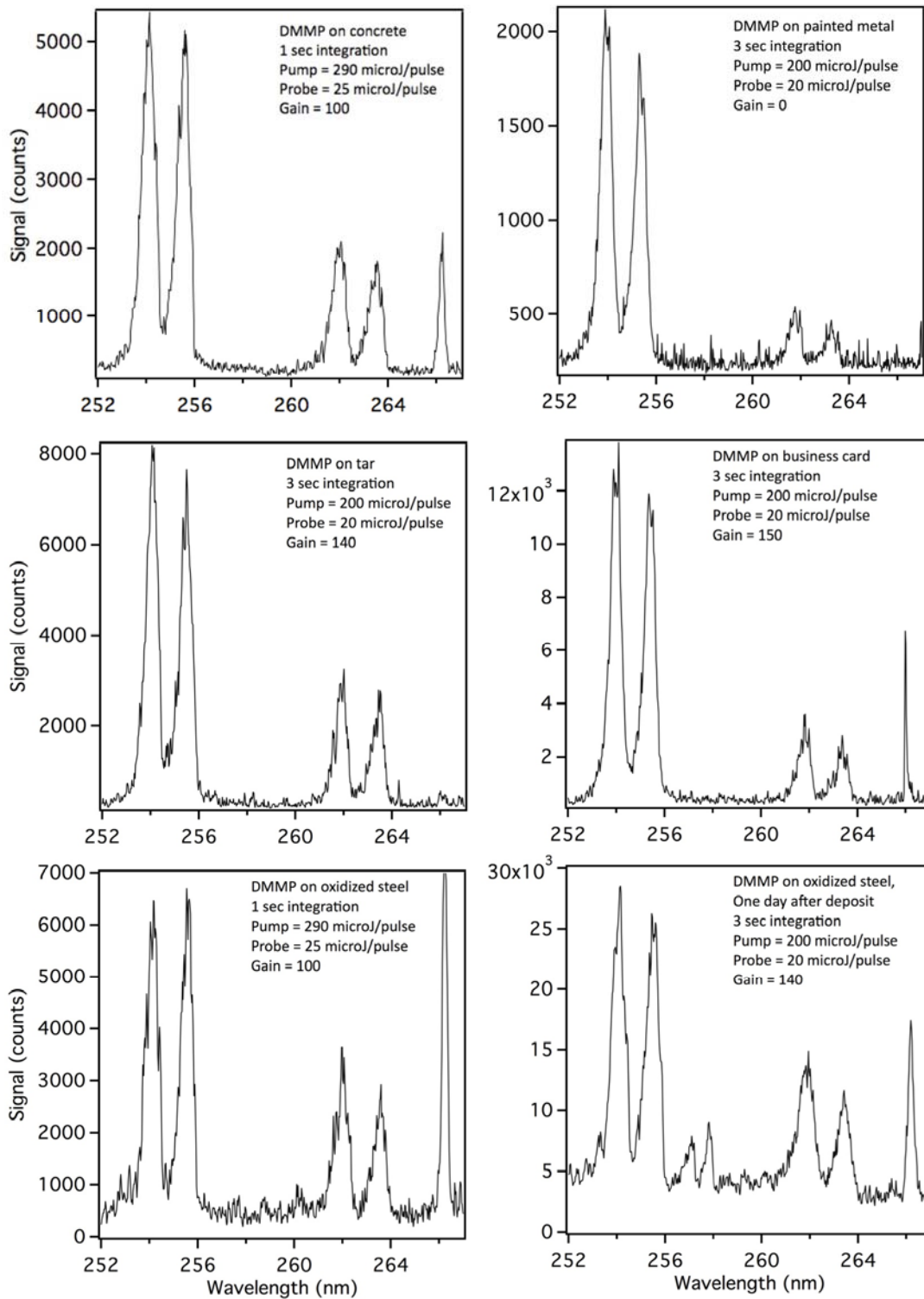
Figure 16 – PF-LIF spectra collected for DMMP simulant deposited on the indicated surfaces and measured for the indicated conditions.
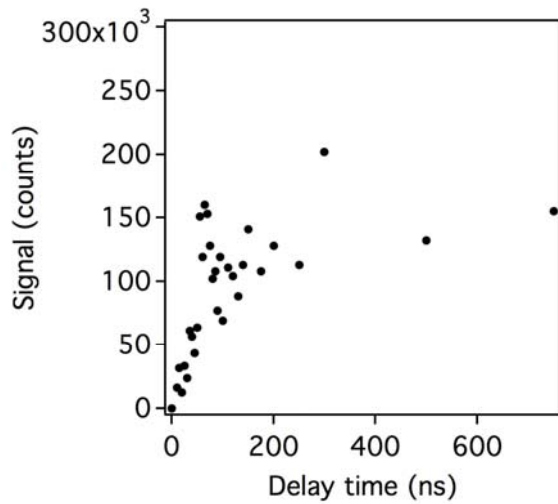
Figure 17 – Dependence of the surface PF-LIF signal on the delay time between the PF and probe laser pulses.
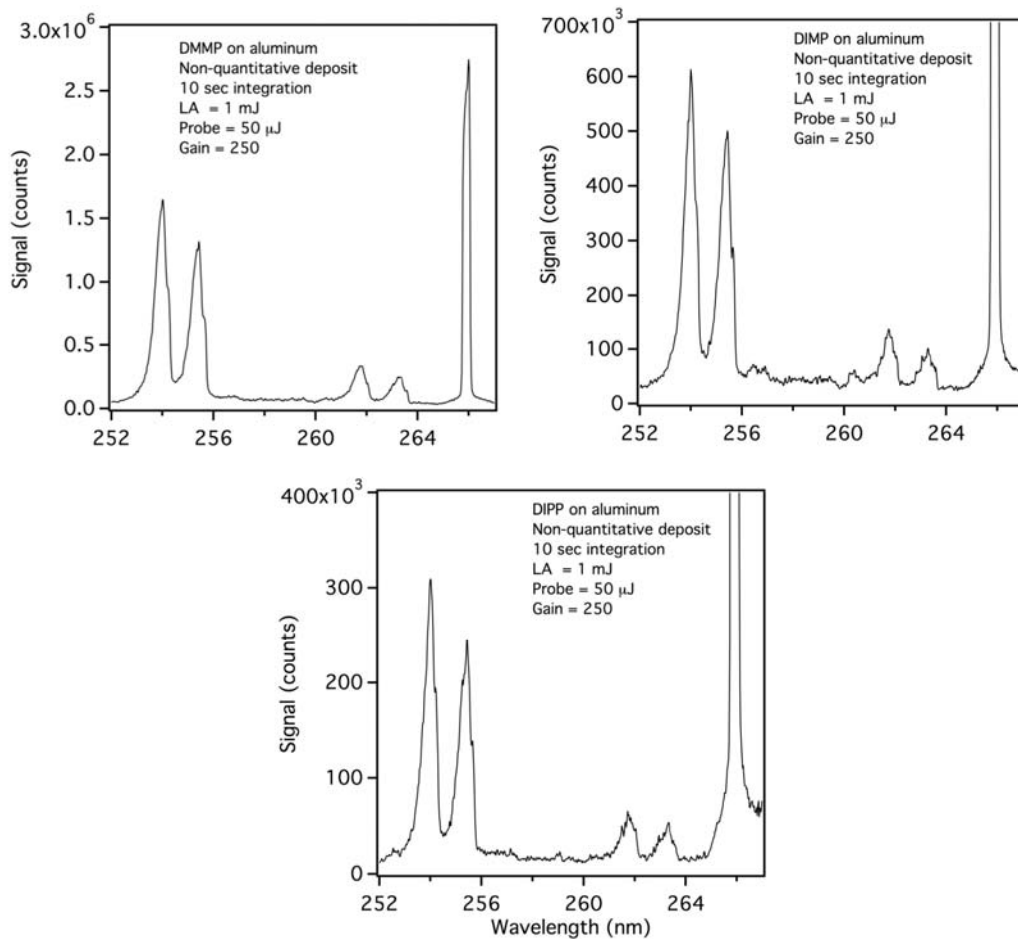
Figure 18 – Surface PF-LIF measurements made of three OP-nerve-agent simulants deposited on aluminum.
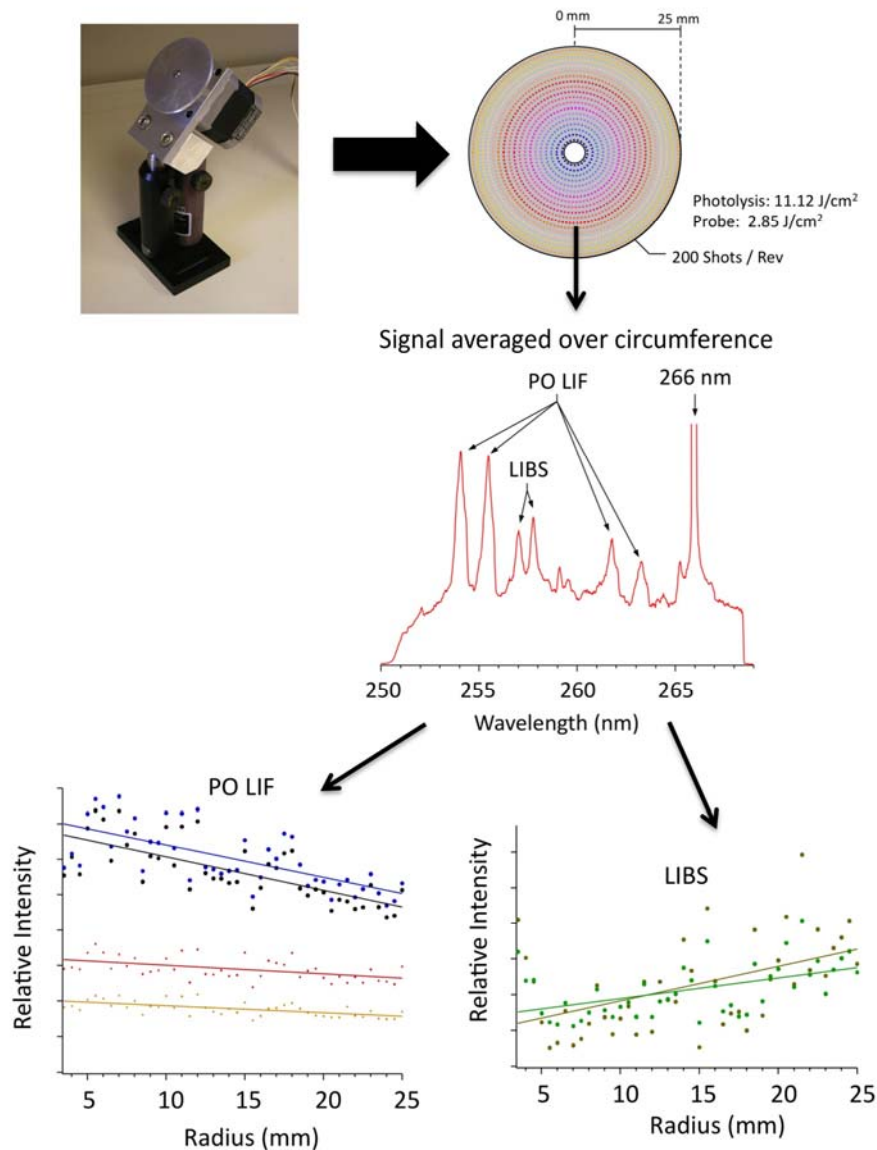
Figure 19 – The PF-LIF mapping process that was applied to characterization of the DIPP distribution produced by the airbrush deposition method on an aluminum disk.

The lower plots in Figure 19 show the relative intensity of the circumferentially integrated PO LIF signal to the Al LIBS signal, plotted as a function of disk radius. The data suggest an anti-correlation between the PF-LIF and LIBS data. This may occur because the energy of the incident PF pulse is dissipated by the analyte coating in locations where it is relatively thick, and is available for ablating the surface matrix where the coating is thin.

Figure 20 shows the results of the mapping process as made on the same coated aluminum disk. The map is color coded according to the apparent DMMP concentration at each point, which is indicated on the color bar. The concentrations were calibrated by allocating the total mass deposited on the disk (1.5 mg, as determined by weighing the disk before and after deposition) according to the PO LIF intensity measured at each pixel. It is clear from the image that the PO concentration distribution produced by the airbrush method is non-uniform and that spatial averaging should be used where possible to reduce concentration errors.
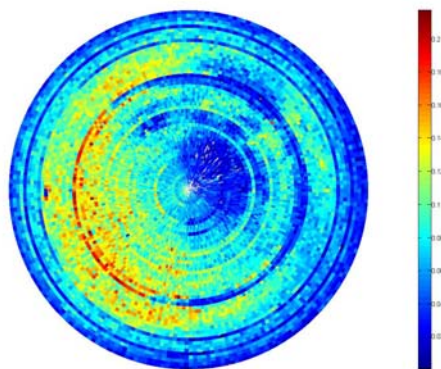
Figure 20 – The DIPP on aluminum concentration distribution generated by the mapping procedure. The colorbar indicates concentration in $\mu g/cm^2$.

After establishment of the deposition method, quantitative PF-LIF measurement of simulants deposited on surfaces was possible. Measurements made on wood, Lucite, and cardboard surfaces are shown in Figure 21. They demonstrate that the indicated concentrations (ranging from 73 to 113 $\mu g/cm^2$) can be measured on realistic surfaces that differ significantly in porosity (which is expected to affect their uptake of the deposited fluid) in a relatively short time (seconds).

5.5 PO generation mechanism

The existence of a visible and audible spark during the PF step indicates the formation of a plasma on the surface being probed. This is consistent with the observation of emission from Al atoms in the spectrum of Figure 19, and with other measurements that show both broadband, thermal plasma emission and narrow-line emission from various neutral or ionic species. For example, the spectra in Figure 22 show aluminum LIBS lines that are affected by plasma Stark shift and Stark broadening at short time (50 ns) after the PF pulse, but not at longer time (1 μs), as the plasma dissipates.

If a plasma is present, one must consider how PO radical is formed and exists in such a harsh environment. It is possible, for example, that the plasma may atomize the entire simulant molecule and that PO is created by the recombination of P and O atoms, rather than by photolysis to release an intact fragment, as is presumed to occur in the gas phase. Such a reaction has been observed by Baudelet et al. [xxiv] when CN is produced by the combination of C and N atoms in a LIBS plasma.

To explore this, we examined the characteristics of a plume formed on a rotating aluminum substrate (both with and without DIPP coating) at short probe delays (10-50ns) after the PF pulse. The aluminum used in this work was an alloy, probably 6061 T6 aircraft aluminum with an oxide layer. The use of an dense aluminum substrate (rather than a porous material like concrete) is expected to constrain heat deposition to a small surface area and, thus, to create a plume temperature and shock-wave intensity that is high relative to that produced on more porous materials. The photolysis energy applied was in the range

of 100's to 1000 μJ, and was deposited in an effective spot diameter of about 74 μm. Even at the lowest photolysis energy, an ablation was audibly and visibly detected. The spectroscopic measurements allowed estimation of the plume instantaneous temperature and composition, and the plasma electron density.   The results are described in the following sections.

5.5.1 Plume temperature measurement

An instantaneous (the plume is radiating strongly and cooling rapidly) plume temperature can be determined by examining the intensity of aluminum spectral lines that originate from widely separated upper energy levels. If local thermal equilibrium (LTE) can be assumed, then the intensity (I) of radiation from a given transition behaves according to:

$$I \propto g \cdot A \cdot e^{-\frac{E}{kT}} \qquad [1]$$

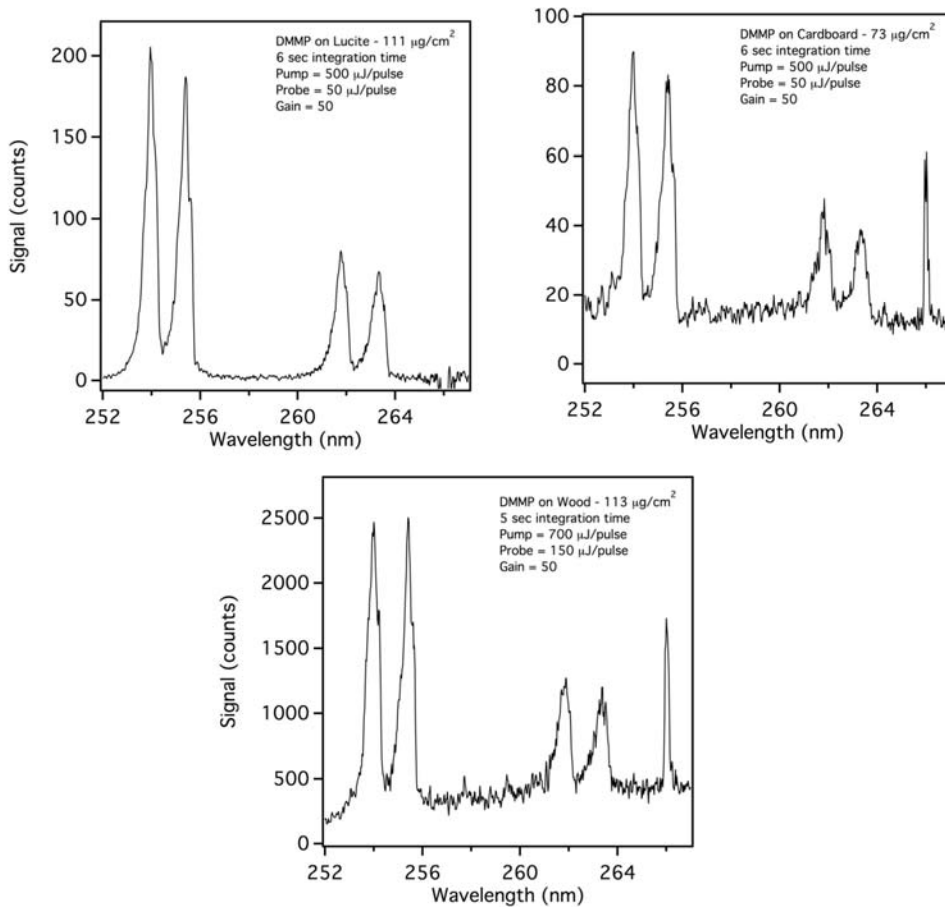Figure 21 – Measurements of quantitative deposits of DMMP conducted on the indicated substrates and at the indicated concentrations.

where E is the energy of the upper level, g is its degeneracy, k is Botzmann's constant, T is the plume temperature, and A is the Einstein "A" coefficient of the transition. If log(I/g·A) is plotted against E for several transitions, the plume electron temperature can be obtained.

30

The intensity in this case is not the peak intensity, but is the integrated line intensity. Since we are interested in determining the initial plume temperature it is important to use emission data acquired as near as possible in time to the photolysis pulse because the plume cools rapidly. In this work we use data acquired at a 20-ns delay. It is also necessary to use emission lines whose g·A products are accurately known – we used some of the stronger, lower-energy aluminum lines whose data are published online on the NIST atomic spectroscopy database website [xxv]. Because most of the emission lines of interest occur as doublets, a fit must be performed to the spectrum to extract the individual linewidths and intensities. In this work we selected emission lines from two well-separated upper levels whose spectroscopic parameters were well known. One line (257.54 nm) originated from the 38929 cm^{-1} level (see Figure 23); the other (396 nm) from the 25347 cm^{-1} level. The identity of the lower level in each transition is not important as long as self-absorption is accounted for. In principle, more lines should be used to determine the temperature – however at such short delays (~10ns), where plasma effects are strong, it is difficult to find well-defined lines to analyze.
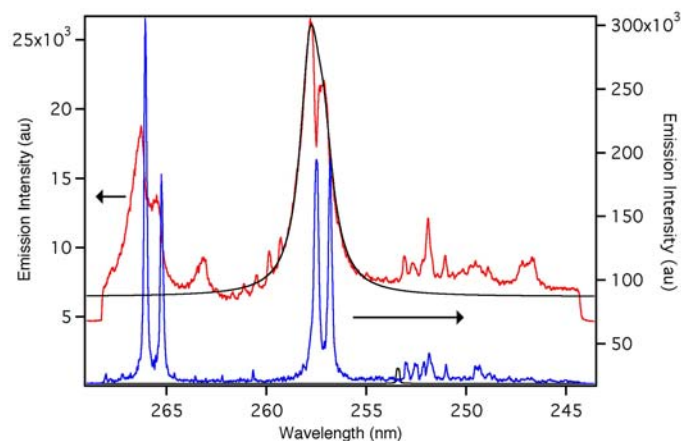
Figure 22 – Emission spectra of Al LIBS lines acquired at 50-ns delay (red) and 1-μs delay (blue). At 1 μs the spectrum appears to be free of plasma Stark shift and Stark broadening.

Based on analysis of the two lines at 257.54 nm and at 396 nm we estimate the temperature at 20 ns delay to be approximately 11,000K. One indicator of the state of PO under this condition is the comparison of the characteristic energy at this temperature (k·T = 91 kJ/mol at 11,000K) to the PO bond energy (about 580 kJ/mol [xxvi]. The fact that k·T is about 1/6th of the bond energy supports the notion that PO may not be fully dissociated. However, there is uncertainty in the temperature because only two transitions was used for the fit, and because cooling may have occurred prior to the 20 ns delay at which the temperature was measured.

5.5.2 Measurement of atomic P and PO radical

Additional information regarding the state of phosphorous in the plume can be obtained by comparing the thermal emission from P atoms to the LIF from PO. The ability to measure both is demonstrated in Figure 24, where spectra are compared that were measured at a 10-ns delay after the PF pulse, both with and without excitation by the probe laser. In the spectra collected without laser excitation, the narrow spectral features near 253 and 255

nm are identified as thermal emissions from neutral phosphorous atoms and the feature at 247 nm is due to emission from carbon. Comparison of spectra collected without laser excitation at different delays shows that both the atomic phosphorous and atomic carbon emission has largely dissipated by 30 ns after the photolysis pulse. This is consistent with the emission rate expected on the basis of the published "A" coefficients (labeled in Figure 24). For both phosphorous and carbon, the transitions occur between two highly excited levels and, once the upper state is depleted, there is no more detectable emission from those atoms (at least in this spectral range).
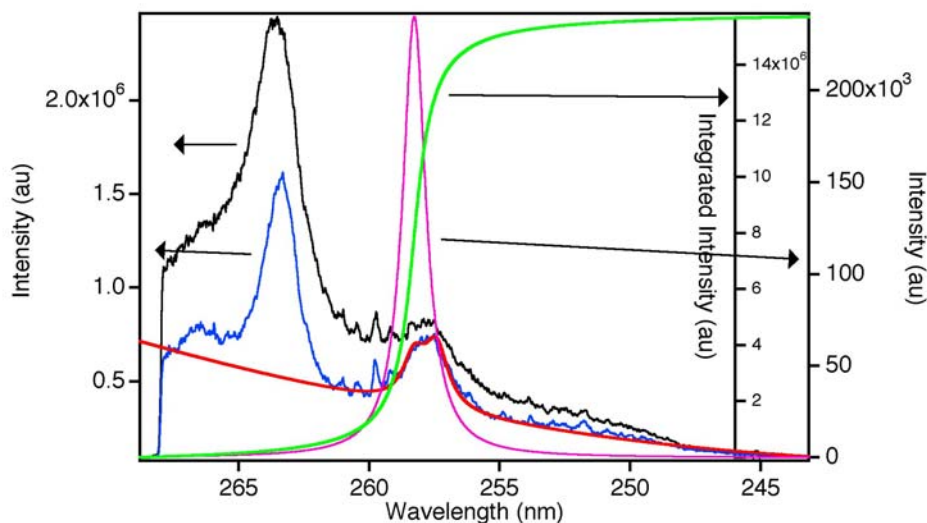
Figure 23 – Plot illustrating the determination of integrated line intensity for the 38929$\rightarrow$ 0 cm^{-1} transition. There are actually three lines (38929$\rightarrow$0 cm^{-1}, 38939$\rightarrow$112 cm^{-1}, 38929$\rightarrow$112 cm^{-1}) at wavelengths of 256.80 nm, 257.50 nm and 257.54nm. The red curve is a fit to all three overlapping lines with the plasma background. The magenta curve is the best fit to the single line at 257.54 nm. The green line is the integrated intensity of the best fit to the 257.54 nm line. This is the intensity that is used in the temperature determination. The lines near 264 nm would actually be a better choice for temperature determination, but their spectroscopic information is not available.

Comparison of the spectra collected with and without laser excitation (at 10-ns delay) in Figure 24 shows that, even at this short time after PF, the probe laser stimulates some PO LIF. Figure 25 and Figure 26 show this in more detail. In order to better discriminate between P and PO emission, the spectra were acquired with a spectrometer slit width of 100 μm. This increased the spectral resolution to the point that rotational band structure in the PO vibronic peaks could be detected and, thus, the PO LIF could be distinguished from the P thermal emission (which, being an atomic species, has no rotational-vibrational structure). The difference in probe-on and probe-off spectra in Figure 25 also suggests that both P and PO are present at 10 ns after the fragmentation pulse. At times later than that, the P signal diminishes and the PO signal increases in strength.

Figure 24 – Spectral emission from the sample plume with and without excitation by the probe laser.

Figure 25 – Comparison of atomic phosphorous emission (without probe laser) and PO LIF emission with the probe laser.

Figure 26 – Temporal evolution of PO LIF signal as a function of time delay between the photolysis probe laser pulses.

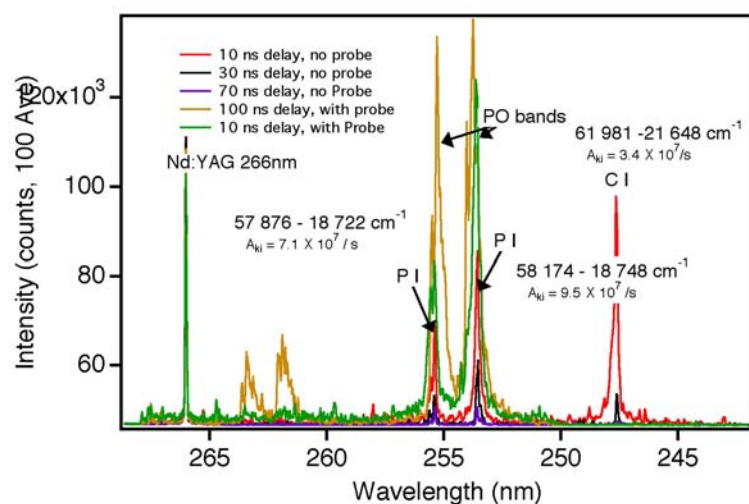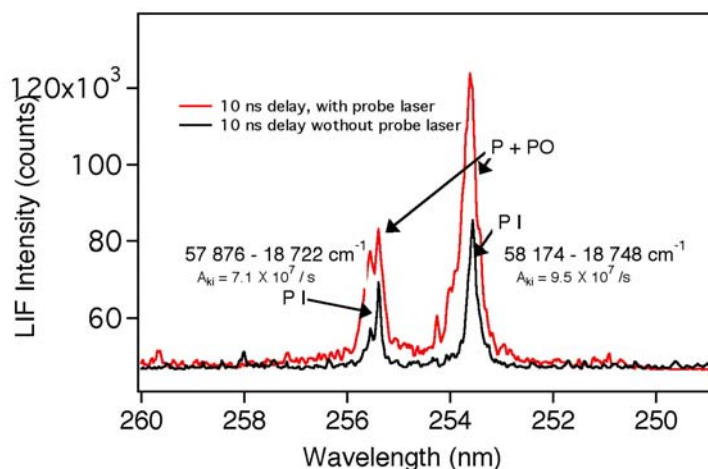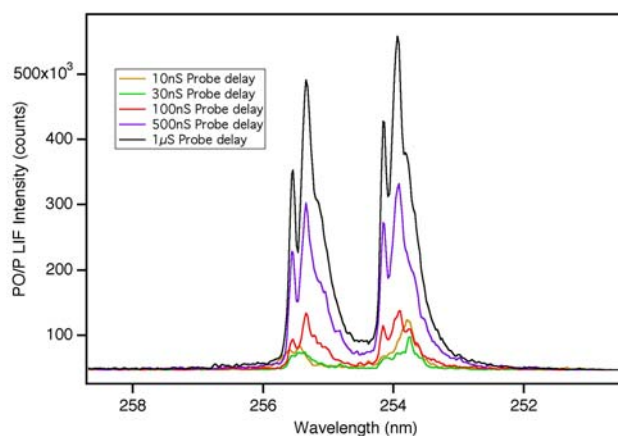The increase in PO emission and decrease in P emission are consistent with a scenario in which phosphorous initially exists predominantly as P atoms and then combines with O to form PO. However, it is not conclusive evidence because it was not possible to quantitatively relate the amount of P initially present to PO present at later times. An alternative explanation for the rise in PO signal is an increase in population of the lower state of the LIF transition over time that results from collisional energy transfer. Sausa et al. [xvi] also observed a rise in PO signal that they attributed to rotational energy transfer to the ground state of the transition. However, their measurements were made at low pressure (10 torr N_2) and showed a relatively fast rise (10's of ns). At atmospheric pressure, the same process would be expected to occur over a much shorter time period than the rise observed by us. On the other hand, significant differences exist between the measurements made here and those made by Sausa. It is clear that a plasma is produced here and it is unlikely that a plasma forms in their vapor-phase measurements. Moreover, the apparent loss of PO with time after the fragmentation pulse (attributed to the $PO+O_2$ reaction) does not appear to occur here (Figure 17). On the basis of these results, it cannot be concluded that the P+O channel is predominant; however, it certainly seems possible.

5.5.3 Measurement of plume spatial dynamics

Additional information regarding the plume dynamics was obtained by making planar laser-induced fluorescence images of the plume using the probe laser pulses. This allowed the plume dimensions to be measured, which provided useful information to determine the optimal size of the probe laser. It also allowed the spatial distribution of PO to be visualized as a function of time, and showed differences in plume temporal evolution that appear to be determined by the matrix on which the simulant is deposited.

PLIF imaging was accomplished using the apparatus of Figure 7, which directly imaged the plume (with a 3x magnification) onto the face of the intensified CCD camera (having a pixel size of 26 μm). The probe laser was formatted into a sheet of 1-cm width and 75-μm thickness, and was typically operated at an energy of 100 μJ/pulse. Spectral filtering of the plume emission was conducted using a bandpass filter that transmits the PO emission wavelengths. Plume images were collected at intervals of 50 ns for delays ranging from 50 ns to 2 μs after the PF pulse. For each delay time, several hundred images were acquired and averaged. Images were made on both Al (relatively non-porous substrate) and concrete (porous substrate). The surface deposits of DIPP were made without quantification for these tests.

Selected images are shown in Figure 27 and Figure 28 for DIPP on concrete and aluminum surfaces, respectively. The concrete data show near-maximum expansion of the plume by a time of 1 μs after the PF pulse, with little additional expansion between 1 and 2 μs. They appear to confirm that measurement at a delay time of 1 μs after the PF pulse is optimal for measurement of PO LIF and indicate that the largest concentration of PO is internal to the plume. Comparison of the DIPP/concrete images to those of bare concrete indicates that the early-time (0-100 ns) emission is predominantly caused by broadband plasma emission for that substrate. At later times, the emission is primarily due to PO LIF.

The PF-LIF behavior on aluminum appears different. At early times, it shows very little plasma emission prior to emergence of the PO LIF signal. Also, the spatial distribution of

PO LIF is most intense at the extremities of the plume (a shell-like structure), rather than the center. The maximum PO LIF emission occurs at approximately 600 ns with a horizontal plume dimension of approximately 660 μm and a vertical dimension of 600 μm. It is possible that the lower plasma emission occurs because of shielding of the surface by the analyte film on the non-porous aluminum substrate (similar to the effect causing the anti-correlation between the PO LIF and the Al LIBS in Figure 19). This would be less likely to occur on the porous concrete surface.

In both cases, the plumes appear to grow to maximum size and to persist in that state for a long period of time (600 to 2000 ns). Ultimately, the PO signal decreases, but the plume does not appear to dissipate as this occurs. It is not clear why this is the case; however, it is possible that the PO is being consumed by conversion to PO_2. Recall that this reaction should be occurring much more quickly than observed at atmospheric pressure. If the P+O reaction is occurring, it may be that recombination occurs at a relatively low rate (thus, gradually producing PO) and that the PO is consumed quickly after this occurs. It might also be that molecular oxygen (required for conversion to PO_2) is depleted in the plume and that the reaction occurs much more slowly for this reason. Finally, it is possible that the probe laser is dissociating PO_2 to release PO , which is excited to fluoresce and is rapidly re-converted back to PO_2.
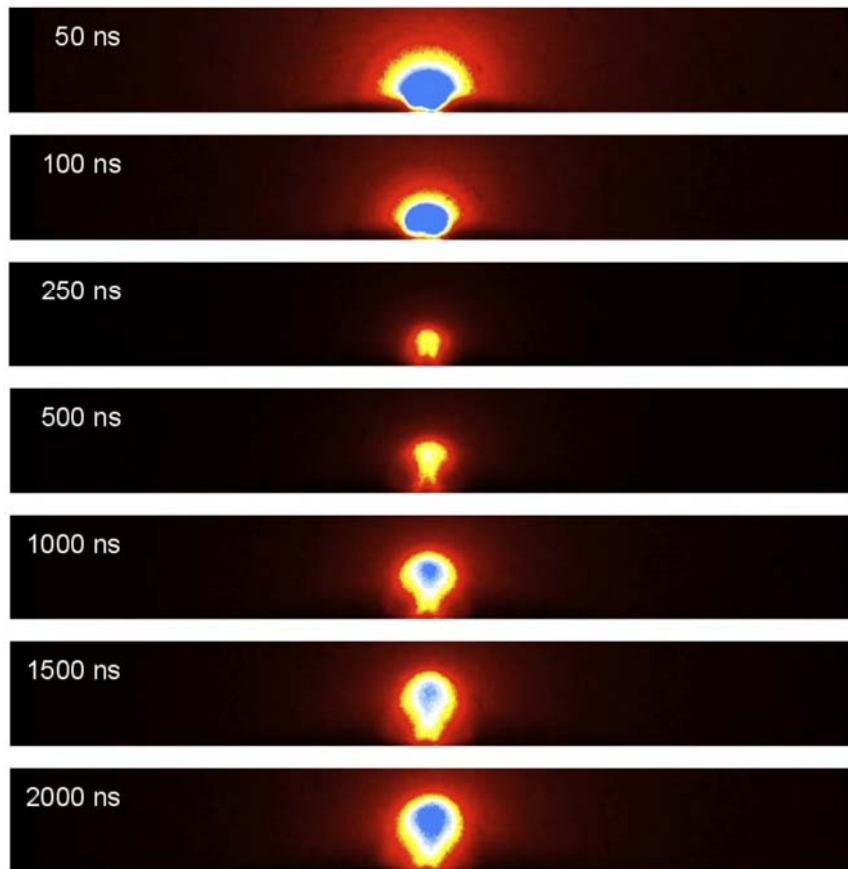
Figure 27 – Image sequence showing the evolution of the plume collected from a sample of DIPP on concrete.
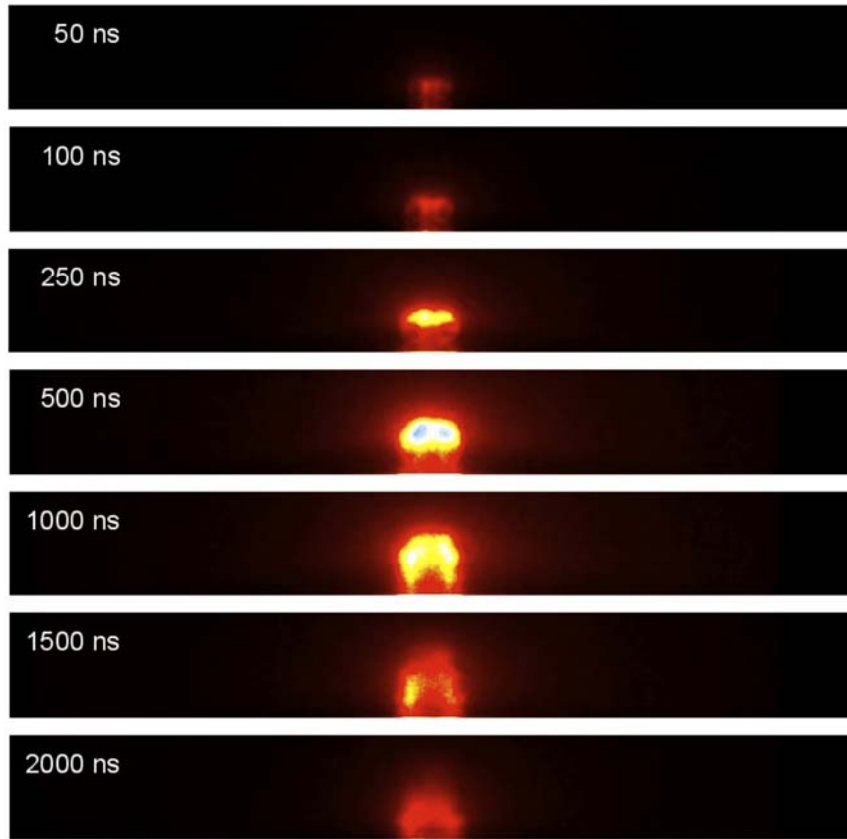
Figure 28 – Image sequence showing the evolution of the ablation plume of DIPP on an aluminum surface.

5.4.4 Plasma electron density

The plume images displayed in Figure 27 and Figure 28 only qualitatively present the extent of the PO fluorescence. No attempt has been made to correct for the spatial intensity profile of the probe beam, or absorption of the probe beam and/or the fluorescence emission. We have, however, evaluated the plasma electron density by measuring the emission line width and its shift in wavelength relative to measurements made without a plasma. The electron density is important because it determines the transmission of light into the interior of the plume. If the electron density exceeds the critical density, then PF or probe laser radiation can be reflected from the plume without exciting PO within it.

Figure 29 shows aluminum emission spectra measured at short (10 ns) and long (200 ns) delay afer the PF pulse. Note the large linewidth and Stark wavelength shift observed at the 10-ns delay. Also evident is a strong self absorption (cooler neutral-Al outer region which absorbs light from the hotter interior region of the plume) which appears in the spectra collected at both times (appearing as dips in the center of each doublet member at 200 ns delay and as dips occurring at wavelengths corresponding to the doublet wavelengths in the 10 ns delay spectrum). Based on the observed linewidths at short delay times we estimate [xxvii,xxviii] that the electron density is $\sim 2 \text{ X } 10^{20}/cm^3$. This is about 100X lower than the

36

critical density at 266 nm (1.57×10^{22}/cm^3) and should, therefore, not affect optical transmission through the plume.

Figure 29 – Neutral aluminum plasma emission at 10 ns (blue) and 200 ns (red) delay between the PF laser pulse and gating of the acquisition system. Lines are viewed in emission without the probe laser. In the 200-ns spectrum, self-absorption is evident at dips whose wavelength correspond to the peaks of the 10-ns spectrum. Dips in the center of each 200-ns doublet member are also caused by self absorption.
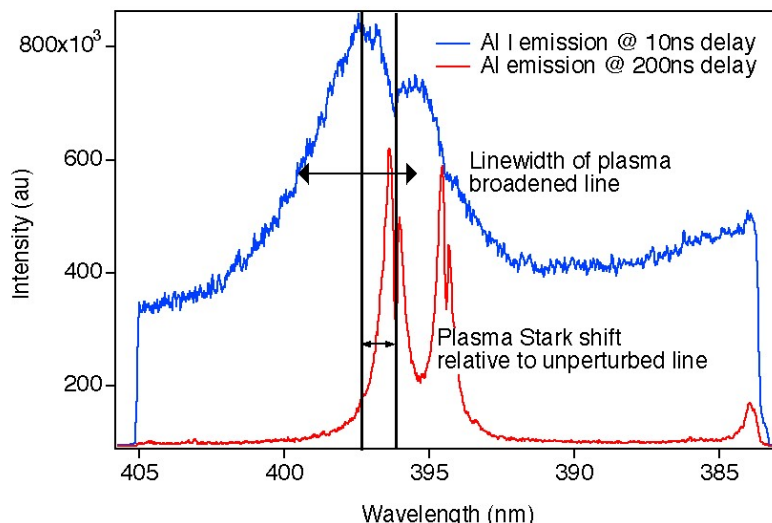
5.6 Determination of a detection limit

The establishment of a quantitative surface deposition method allows the PF-LIF detection limit to be determined. The calibration of the sensitivity of a chemical measurement is usually accomplished by varying the analyte concentration in a controlled manner and measuring the resulting signal strength. The calculation of the detection limit then requires either comparison of this sensitivity calibration to sources of uncertainty, such as the background level [xxix] or, if false positives are a concern, the use of the ROC curve formalism to relate the probability of detection to the associated false positive rate [xxx, xxxi]. Regardless of how the detection limit is defined, a sensitivity calibration is most directly performed using well-defined analyte concentrations. For example, to quantify the detection of a gas-phase species, a common approach to control the analyte concentration is to vary the feed rate of the analyte vapor into a flow-cell [xxxii]. Alternatively, the feed rate might be held constant, allowing systematic evaluation of other experimental parameters (e.g., the laser pulse energy) to be conducted while maintaining a constant analyte concentration [xxxii].

In contrast to the above example of a well-mixed gaseous sample, chemicals deposited on surfaces are more difficult to evaluate quantitatively. Specifically, (1) the deposition of the chemicals is typically inhomogeneous and substrate-dependent, (2) the surface itself often possesses significant irregularity, affecting the signal strength, and (3) the measurement approach can alter the chemistry and morphology of the sample, so repeated probing of the same spatial location will lead to different results. To be clear, these characteristics are not just artifacts of our specific deposition approach, but would be expected in any realistic chemical deposition. As previously discussed in this report, we took specific steps to

address these three challenges. The air-brush deposition provides a reasonably even concentration over ~50% of the substrate surface. Gravimetric measurement of the deposited mass allows calculation of the mean chemical concentration on the surface by dividing the mass by the surface area over which the deposition occurs. The substrates are prepared to have smooth surfaces to minimize irregularity, and the samples are rotated during the measurement so that each single-pulse-pair measurement probes a different spatial location.

When measuring a sample of DIPP deposited on a substrate, 600 individual spectra were typically acquired for each run, and several runs were acquired on each sample. Between each run, the sample was translated so that a circumference at a different radius would be probed. Figure 30 displays 600 individual spectra acquired in a run when probing DIPP on an aluminum substrate. If scattered light from the probe laser is eliminated by the rejection filter, it is expected that the spectrum collected at each measurement location should consist of three major components: (1) the PO-LIF signal, (2) scatter from the 266-nm PF laser, and (3) LIF from other chemical constituents. Assuming that these components vary independently in relation to each other, we can separate them through linear unmixing algorithms. Isolation of the PO-LIF spectral component is desired because it is used to calculate the detection sensitivity.
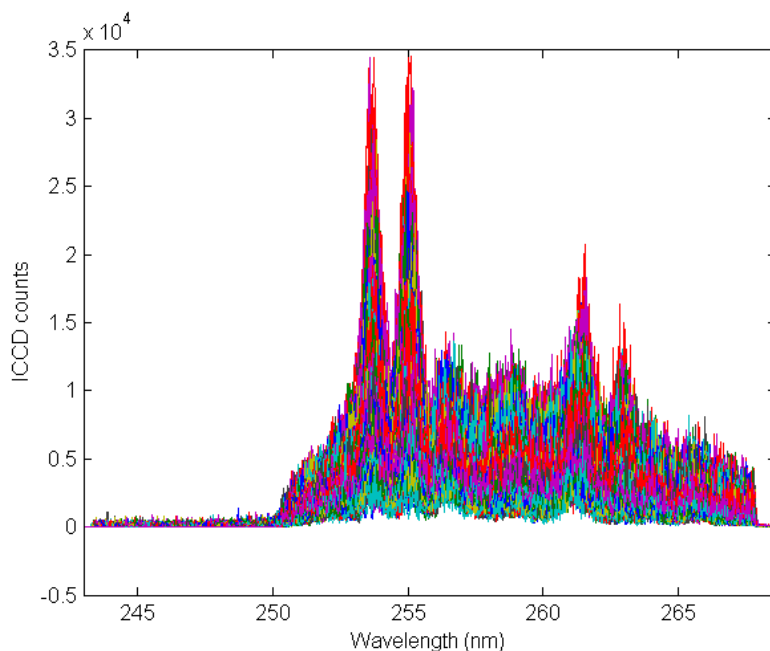
Figure 30 – The set of 600 single-pulse-pair, independent-spatial-location spectra acquired for DIPP deposited on an aluminum substrate. The background counts have been subtracted from these spectra.

In the assessment of the ensemble of spectra, the Sandia-developed runAxsia software [xxxiii] was used to perform multivariate curve resolution (MCR) to separate the PO-related signal from the background. MCR is a numerical approach based on least squares analysis in which the pure component spectra are treated as variables. By limiting the number of pure components, and by placing physics-based constraints on the component spectra and

their relative concentrations (such as requireing non-negative concentrations), an ensemble of mixture spectra can be decomposed into likely pure components. For the aluminum substrate, we find that scatter from the 266-nm pump laser is not a significant component, so we separate the acquired spectra into only two components, the PO-LIF signal and background emission. We note that the background emission is undoubtedly a combination of multiple components, and that we treat it as a single component only for the purpose of separating it from the PO signal. The left column of Figure 31 displays the mean spectra for four different runs on aluminum, as well as the two components determined from MCR analysis. The MCR analysis demonstrates that the PO LIF signal does not vary independently; rather, a portion of the background co-varies with the PO fluorescence features (see the left side of Figure 31).

Figure 31 – <u>Left column</u>: Mean spectra (top), PO-LIF pure components (middle), and background components (bottom) for four runs on a sample of DIPP on an aluminum substrate. The Run 1 results correspond to the single-shot data displayed i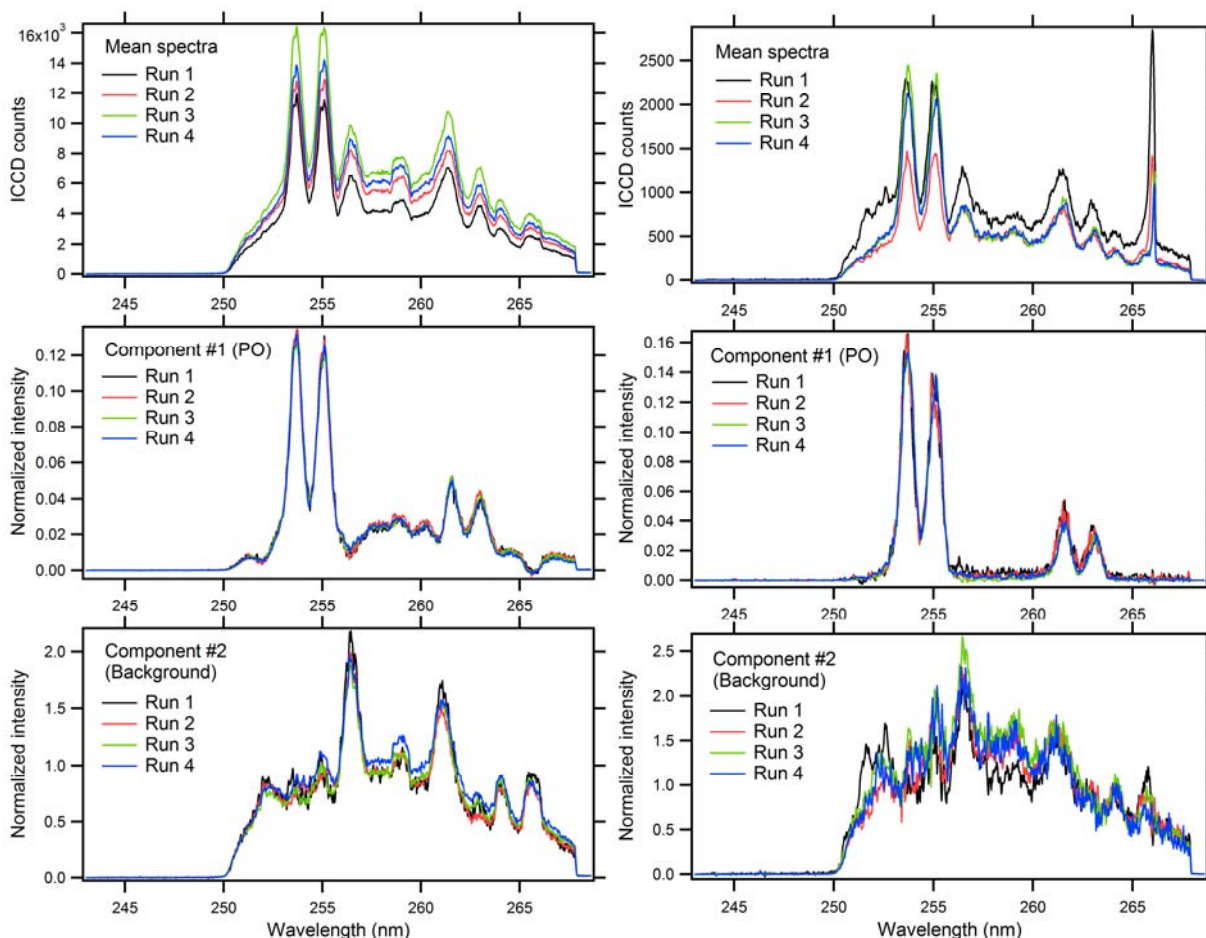n Figure 30. <u>Right column</u>: Mean spectra (top), PO-LIF pure components (middle), and background components (bottom) for four runs on a sample of DIPP on a concrete substrate. While the component corresponding to laser scatter is included in the analysis, it is not displayed.

A similar analysis was performed on the data for DIPP deposited on a concrete substrate. For these spectra, the 266-nm pump scatter is significant, and so the spectra are decomposed into three components instead of only two. The right column of Figure 31 displays the four mean spectra and the decomposition into pure components. Noticeably different than the pure-component PO-LIF spectra measured on aluminum, the PO-LIF pure component spectra associated with the concrete substrate are unaccompanied by other emission features.

While the spectral decomposition provides insight into the nature of the measured signals, its ultimate purpose is to allow the DIPP detection limit to be estimated. This estimation is made using the relative concentration of the PO-LIF component, which is another result of the MCR analysis. Figure 32 displays the relative concentration of the PO-LIF pure component for all 600 of each of the four runs on aluminum and concrete substrates. Because the sample is rotated during the measurement, each of these runs can be considered a spatial scan at a constant distance from the point of sample rotation. It is worth noting how different the measured DIPP depositions on aluminum and concrete appear. The deposition on aluminum varies in a relatively smooth fashion – so much so that a spatial gap in the deposition is evident on Runs 2-4. In contrast, the DIPP deposition resembles individual droplets, likely because much of the film of DIPP has been absorbed by the substrate, leaving only isolated areas where material remains at high concentration.
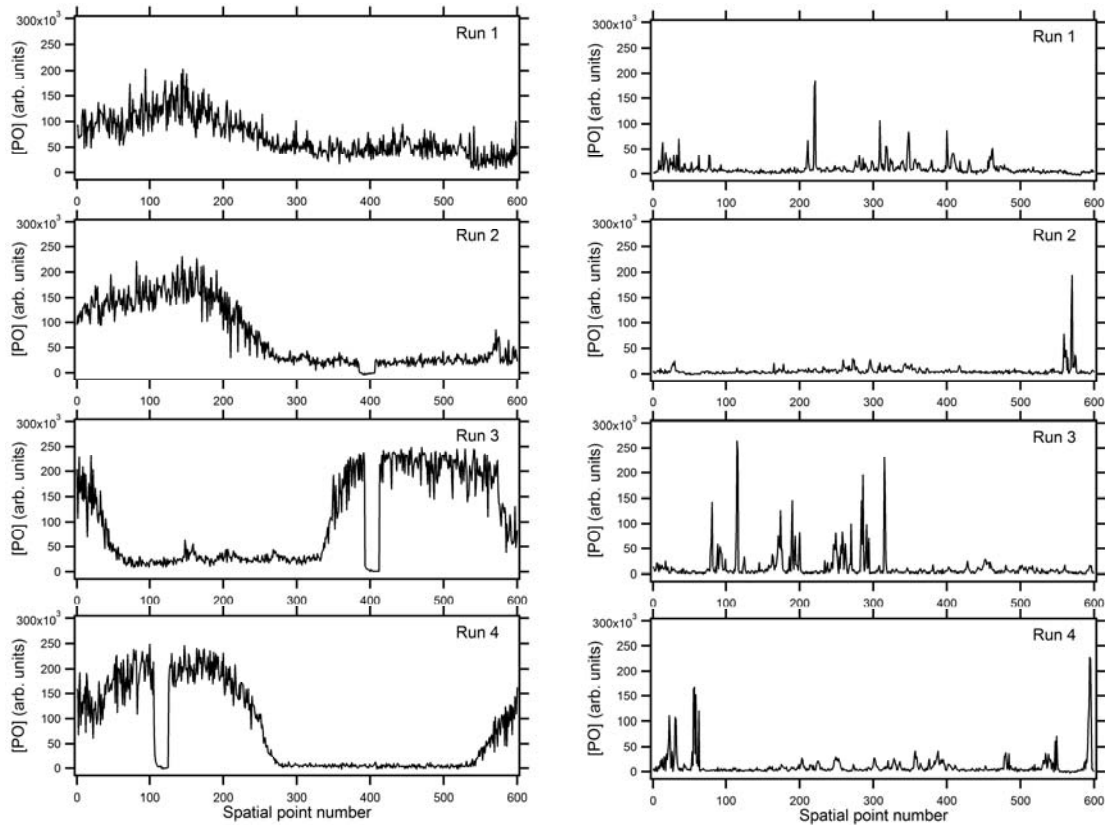

Figure 32 – <u>Left column</u>: Relative DIPP concentration as calculated with MCR on data from four runs on the aluminum substrate. <u>Right column</u>: Relative DIPP concentration as calculated with MCR on data from four runs on the concrete substrate.

Assuming that the amplitude of the PO-LIF component is linearly proportional to DIPP concentration at each location probed, it seems reasonable to approximate the *mean* amplitude of the PO-LIF component as corresponding to the *mean* concentration of DIPP deposited (which is calculated, using the gravimetric analysis, to be 70 µg/cm^2 for both aluminum and concrete). A spectrum corresponding to this mean was selected, allowing a specific spectrum to be related to an estimated concentration.

Using the appropriate spectra in conjunction with knowledge of the counts-to-photoelectrons conversion of the ICCD, it was found that a concentration of 70 µg/cm^2 DIPP on aluminum produces a signal of 2800 photoelectrons for measurement by a single pulse-pair, while on concrete the same DIPP concentration produces a signal of 400 photoelectrons per pulse-pair. But this calculation is only the first step: to assess a detection limit from this information, a criterion for an acceptable signal-to-noise ratio (SNR) is required. The value selected was an SNR of 20, which was found to be a reasonable threshold for detection in past lidar work performed by our group.

In seeking general guidelines for calculating detection limits, it is assumed (1) that the SNR is governed by photon counting statistics, and (2) that the number of fluorescence background photons B is equivalent to the number of fluorescence photons S, scaling linearly with the concentration. From the first assumption,

$$\text{SNR} = S / (S+2B)^{1/2}, \qquad [2]$$

while from the second assumption, $S = B$, so that

$$\text{SNR} = (S / 3)^{1/2} \qquad [3]$$

If an SNR = 20 is required for reliable detection, then $S = 3 \times 20^2 = 1200$. Then the single-pulse-pair detection limits $DL_{1 \text{ pulse pair}}$ are

$$DL_{1 \text{ pulse pair, aluminum}} = (1200 / 2800) \times 70 \text{ µg/cm}^2 = 30 \text{ µg/cm}^2 \qquad [4]$$

$$DL_{1 \text{ pulse pair, concrete}} = (1200 / 400) \times 70 \text{ µg/cm}^2 = 210 \text{ µg/cm}^2 \qquad [5]$$

The various assumptions and extrapolations required to calculate detection limits often leave room for doubt concerning the fidelity of the reported result. To close the loop and check the result of these calculations, in Figure 33 we plot spectra for both the aluminum and concrete substrates which correspond to these detection limits. While the noise is significant, there is definite visible evidence of the PO spectra, and we believe these concentrations can reasonably be assigned to high-confidence detections. It should be emphasized that these detection limits correspond to measurement with a <u>single pulse pair.</u> The requirements of an application generally will not specify numbers of pulses but, rather, a more practical metric such as measurement time per point or rate of scanning of an area. Because the relatively modest energies used in the PF-LIF measurement can be generated at high repetition rates (kHz), it is likely that many pulses can be used to make a measurement in most applications. The signal obtained from these pulses can be averaged to increase the SNR by $N^{1/2}$, where N is number of pulses averaged. As indicated in Equations 3 and 4,

however, the detection limit scales linearly with N. Assumptions made regarding the needs of users and how the method performance compares to them is provided in the next section
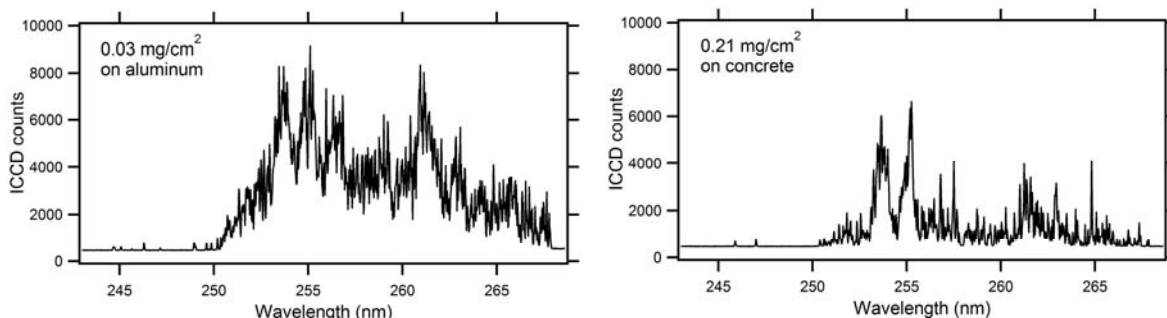

Figure 33 – <u>Left</u>: Spectrum acquired with a DIPP concentration corresponding to the calculated detection limit of 30 μg/cm2 on an aluminum substrate; <u>Right</u>: Spectrum acquired with a DIPP concentration corresponding to the calculated detection limit of 210 μg/cm2 on a concrete substrate.

5.7 Relationship of sensitivity and speed to application metrics

The value of the method can be estimated by comparing its performance to the needs of users. Two types of applications were considered: (1) a rapid scan that would use PF-LIF to quickly search for areas of contamination; and (2) a "swipe substitute" in which PF-LIF would be used to raster scan across an area (10 x 10 cm) that is equivalent to that from which a swipe sample is normally collected for subsequent lab analysis. There are no commerically available optical scanning devices to compare to, so metrics were obtained from consultation [xxxiv] with the Department of Homeland Security (DHS), which had previously released a Broad-Agency Announcement (BAA) for a standoff sensing system. The metrics for swiping were obtained using the U.S. Environmental Protection Agency (EPA) clearance-target criterion [xxxv] for VX contamination (the concentration at which a facility would be considered "cleared" for occupation after a decontamination procedure).

Table 2 contains a comparison of the assumed user metrics to the extrapolated performance of potential PF-LIF implementations. Two scanning formats are assumed. The "Rapid Scan" assumes full-bandwidth scanning (i.e., no signal averaging) so that separate points on a surface are measured at a 1 kHz rate. The "Intermediate Scan" assumes scanning with the amount of signal averaging allowed to meet the DHS criterion (1000 point average allowed to generate a 1-second DHS response time). In all cases, the detection limit is assumed to be reduced in direct proportion to the inverse of the number of measurements averaged (as in Equations 3 and 4, above). It is also considered that the measurement area would have to be moved to probe a fresh surface area at every collection because the measurement depletes surface-borne analyte. The "Swipe" scenario assumes that the probe region is raster-scanned across a grid of 100 x 100 points on the target in a time period of 10 s, and that these points are averaged to generate a concentration reading for that area. The requirements for this mode are somewhat arbitrary because it is meant to replace a process that currently takes several days to accomplish (i.e., material swipe collected and sent to lab for analysis). Thus, a measurement period of minutes would still offer a large advantage.

Some other assumptions made in this extrapolation can be pointed out. First of all, it is assumed that the concrete and aluminum detection limits are representative of mean measurements made on the surfaces and that the averaging of multiple measurements will scale directly with the number of measurements. In cases where the distribution of agent is extremely spotty (such as in the case of concrete in Figure 32), this assumption might break down for short numbers of averaged pulses, in which high signal spikes are not sampled. It is more likely to be accurate for averaging of large numbers of pulses, such as in the swipe simulant, or when broad areas are scanned.

Other conditions must be considered which affect the choice of a practical implementation of the PF-LIF approach. These include the operating standoff range and its effect on signal level and hardware specifications. This discussion will be deferred until the later section, which deals with the characteristics of a PF-LIF instrument.

Table 2 – Comparison of extrapolated PF-LIF performance to assumed metrics

Substrate	Rapid Scan		Intermediate Scan		"Swipe"	
	Duration (s)	Detection limit (μg/cm^2)	Duration (s)	Detection limit (μg/cm^2)	Duration (s)	Detection limit (μg/cm^2)
Aluminum	10^{-3}	30	1	0.03 **(0.01X)**	10	0.003 **(8X)**
Concrete		210		0.21 **(0.07X)**		0.021 **(58X)**
Metrics			**1**	**3**	*****	**0.00036**

The results in Table 2 indicate that the PF-LIF method should be able to meet the needs of a DHS-scanning system by a wide margin (sensitivity 14-100 times better than needed at a measurement period of 1 second). The results also show that, for a 10 s collection, the sensitivity on a non-porous surface (like aluminum) would fall short of meeting the clearance requirements by a factor of 8X. For a porous surface (concrete) they would fall short of clearance by 58X. The measurement could be improved further by averaging (a direct linear scaling would indicate, for example, that the on-concrete clearance level could be reached with 580 s of averaging time). A measurement time of ~10 minutes is not unreasonable, given that swipes are normally sent for lab analyses, which can take several days.

5.8 False alarms on phosphate materials – use of PF-LIF as a trigger

While PF-LIF offers a means to rapidly scan surfaces for for OP LVAs at a sensitivity and rate that is relevant to the needs of customers, the reliance on only the PO group as an indicator of LVA presence exposes PF-LIF to the possibility of false alarms. The fact that none of the matrix materials that were measured showed PO signal suggests that detectable levels of PO in common surfaces are not ubiquitous; however, it is likely that certain other matrices or coatings will eventually be found to be problematic. This was proven by measuring a phosphate-containing detergent (Betco Corp), which showed (Figure 34) clear PF-LIF signal from its phosphates.

False alarms can be mitigated by using PF-LIF as a rapid trigger for a more discriminating sensor. In this architecture, the trigger provides high measuremental speed and sensitivity while the confirmer provides selectivity. Because the confirmer is used infrequently, it is acceptable for it to take long to make a measurement. A trigger-confirmer arrangement is

used in bioaerosol threat sensing, where the trigger may be a low-specificity fluorescence-based particle sensor and the confirmer would be an antibody or DNA-based sensor. For LVA detection, the confirmer could be a fieldable mass spectrometer coupled to a surface sample (such as the Direct Analysis in Real Time (DART) [xxxvi] or Desorption Electrospray Ionization (DESI) [xxxvii]. Alternatively, as discussed in the following sections, it could be an optical method, such as Raman spectroscopy.
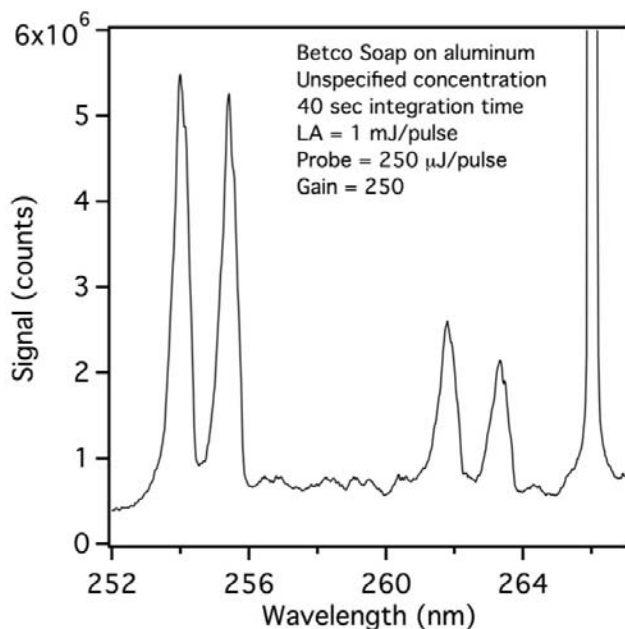

Figure 34 – PF-LIF measurement made on Betco phosphate-containing soap.

5.9 Raman spectroscopy as a potential confirmatory channel

Raman spectroscopy is a potential method to use in confirming a detection. It measures the full vibrational spectrum of an analyte and, thus, indicates the presence of more bond types than just PO. Its use is highly compatible with PF-LIF because both can be performed using the same instrumentation. Moreover, because Raman is being developed commercially for LVA detection (ITT Corporation LISA system [xxxviii]), a pathway exists to manufacture a combined PF-LIF/Raman system. Raman is, however, less sensitive than most LIF-based methods. This can be compensated for, to some extent, for by accumulating a signal for a longer time period (because Raman would only be used after PF-LIF "hits"). Nonetheless, it would need to be proven sensitive enough to meet the needs of the confirmation role. Some tests were conducted in this project to compare the performance of Raman to PF-LIF; they are described in the following sections.

5.9.1 Distinguishability of phosphate soap from simulants using Raman

Raman spectra were measured on thick layers of three simulants (DIMP, DIPP, and DMMP) and the results are shown in Figure 35. The upper axis shows the wavelength of the emission and the lower axis indicates the Raman frequency shift relative to the excitation laser. For comparison, the Raman spectrum of Betco soap is also plotted. The data were

collected using the 248-nm beam of the PF-LIF apparatus as in the right side of Figure 6. The data consist of various "fingerprint" vibrational bands at frequencies between about 400 and 1800 cm^{-1} and the strong C-H stretch bands at frequencies of about 2900 to 3000 cm^{-1}. It is evident that the spectra should be distinct enough to allow discrimation among these materials.
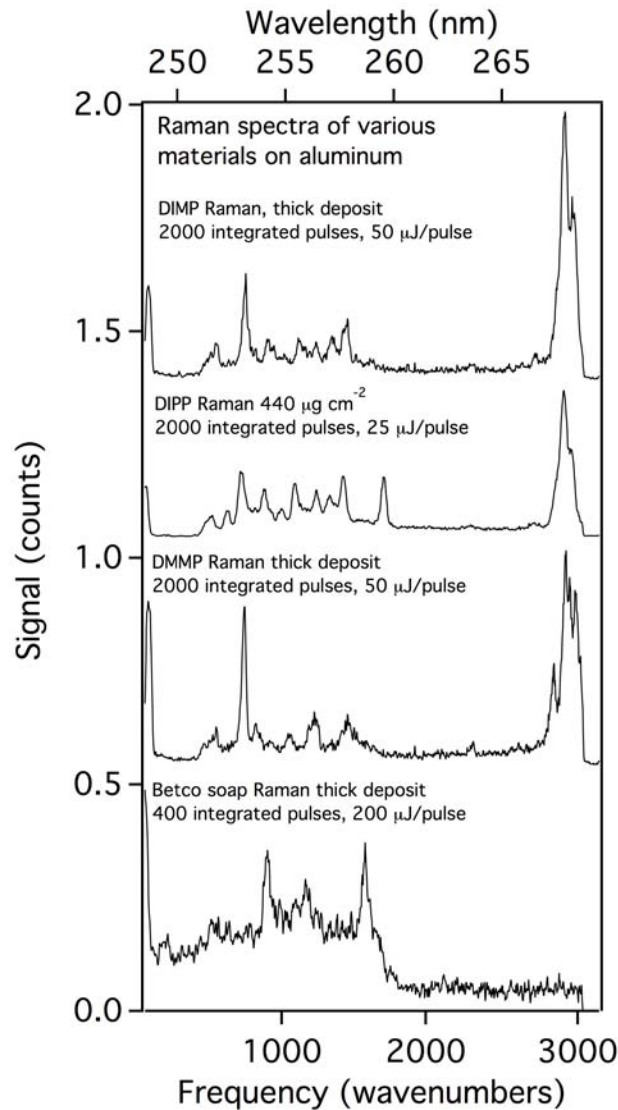
Figure 35 – Raman spectra of thick layers of DIMP, DMMP, DIPP and Betco phosphate-containing soap, as measured by the PF-LIF apparatus.

5.9.2 Raman detection of DIPP on aluminum – airbrush deposition

The ability to detect airbrush-deposited surface films of DIPP using Raman scattering was tested in a similar manner to the PF-LIF measurements. Measurements were made using only 248-nm excitation of samples that were mounted with their normal at 45-degrees to laser incidence (see right side of Figure 6) and which were rotated during measurement. Measurements were also made using PF-LIF in order to compare its performance to that of Raman.

Figure 36 contains spectra collected from a sample of DIPP deposited on aluminum at a concentration of 190 μg/cm². The upper two spectra of the left panel are Raman measurements measured using 25 and 50 μJ of laser energy per pulse. The lower spectrum is a measurement of a "cleaned" aluminum sample. In each case, the signal from 3000 laser pulses was integrated. Subsequent inspection of the data showed that the "clean" sample was not really clean, as evidenced by apparent PO peaks at 256.1 and 254.6 nm. An expanded version of the clean Al spectrum is shown in Figure 37, where it is compared to the spectrum of a more carefully cleaned surface (shown in blue). From comparison of the two spectra, it is clear that the first sample was contaminated by DIPP, which was producing PO radical emissions at bot the 0→1 and 0→2 wavelengths (see the right side of Figure 37). This observation is interesting because it shows that PF-LIF of DIPP can be accomplished with a single laser pulse, although the sensitivity is likely not as high as the two-pulse measurement.
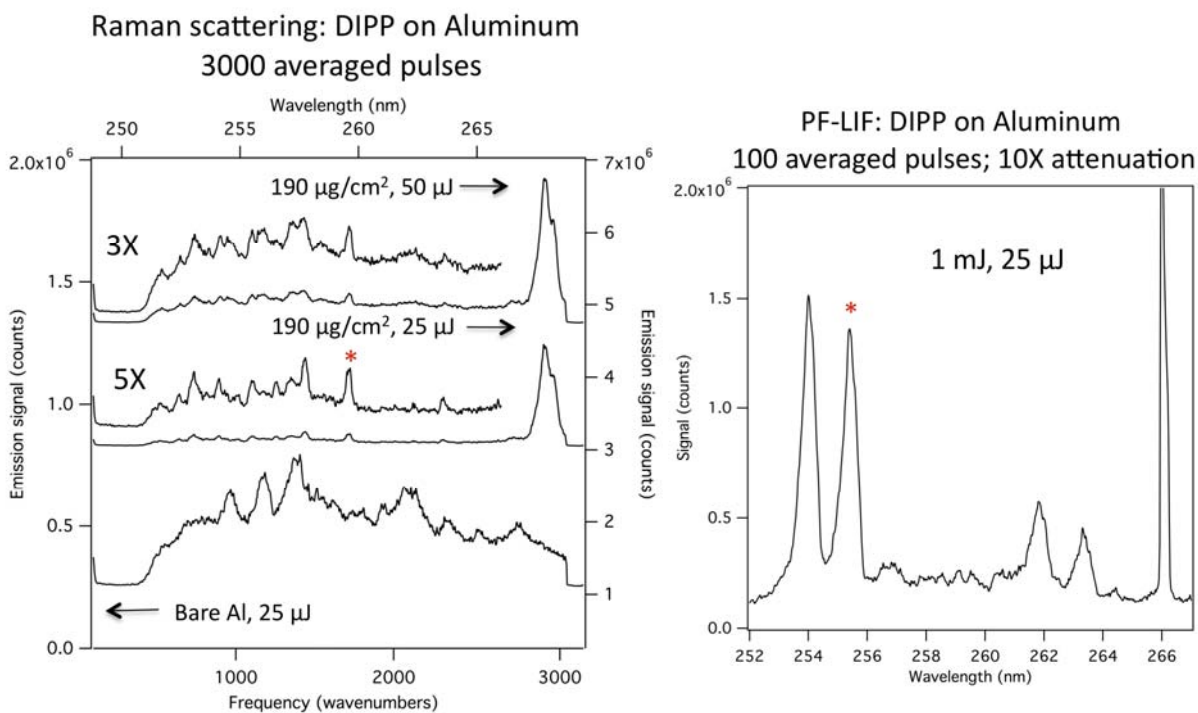
Figure 36 – Left: Raman signals of DIPP on Al and "cleaned" Al. The DIPP was deposited at a nominal concentration of 190 μg cm⁻² and measured using 25 and 50 μJ/pulse. Right: PF-LIF measurements made on the same sample, using a PF energy of 1 mJ/pulse and a probe energy of 25 μJ/pulse. A 10X attenuator was placed in the signal path for this measurement.

The Raman spectrum collected at 25 μJ pulse energy is the same as that measured for a very thick coating of DIPP (Figure 35). The spectrum measured at 50 μJ is, however, different. Comparison of all three Raman datasets shows that the 50-μJ spectrum appears to be a linear superposition of the 25-μJ DIPP Raman spectrum and the spectrum of the "cleaned" aluminum surface. This is made more clear in Figure 37, which shows expanded versions of those spectra and dashed lines to indicate the position of the bare Al features in the 50-μJ dataset.

The behavior of the 190-µg/cm² DIPP-on-Al system seems consistent with a situation in which a low excitation energy (25 µJ/pulse) produces a pure DIPP Raman spectrum and higher energies (≥50 µJ/pulse) produce a mixed spectrum that involves contributions from the aluminum surface. Apparently, a portion of the mixed spectrum is due to single-wavelength PF-LIF of the PO. The remaining peaks in the spectrum may be due to Al LIBS (both broad-band emission and broadened line emission). This is supported by the comparison to a LIBS spectrum of Al (green curve in the left graph of Figure 37, taken at a longer delay after the ablation pulse) which shows Al lines near 257.8 and 266.3 nm that correspond to features in the DIPP-Al spectrum.
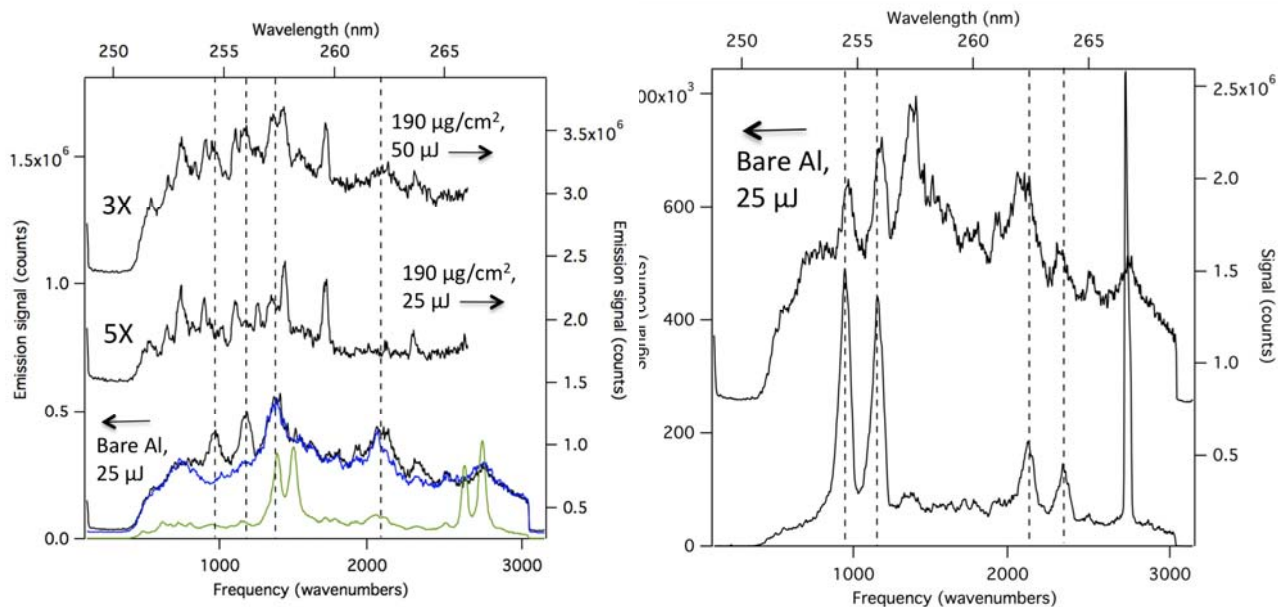

Figure 37 – Left: Expanded view of the Raman spectra of Figure 36, accenting the apparent contribution of the bare Al spectrum to the spectrum collected at 50 µJ. The bottom spectrum shows a superposition of the contaminated Al spectrum with the more carefully cleaned sample (in blue). It also shows a LIBS spectrum of Al (in green) ; Right: Comparison of the DIPP PF-LIF spectrum to the bare Al Raman spectrum.

5.9.3 Signal level comparisons between Raman and PF-LIF

The data shown in Figure 36 can be used to compare the PF-LIF and Raman signal intensities for the same sample. This was done using the peaks marked with a red asterisk. A "fingerprint" Raman feature was selected instead of the C-H stretch because those weaker features must be measured for agent confirmation. The Raman measurement produced 35 counts of signal per laser shot, whereas PF-LIF produced 1.14×10^5 counts per pulse pair. Thus, the PF-LIF measurement produced 3260 times the signal of Raman, per laser shot for the indicated conditions.

5.9.4 Raman detection of DIPP on aluminum – inkjet deposition

After the inkjet deposition apparatus was set up, it was used to repeat the DIPP/Al measurements. Figure 38 contains a plot of the PF-LIF measurements in the range of 253-257 nm (containing the $0 \rightarrow 1$ transition peaks). It is an overlay of 300 spectra collected as

the sample was rotated.   Each was generated using a single pair of laser pulses (1 mJ PF pulse; 25 μJ probe pulse) and with a 10X neutral density filter in place (actual signal is 10X that displayed) to prevent saturation of the ICCD array. The DIPP concentration on the sample was 74 μg/cm². The results demonstrate that the inkjet method of deposition creates a surface deposition that is much more uniform than that of the airbrush (see Figure 20 and Figure 30).
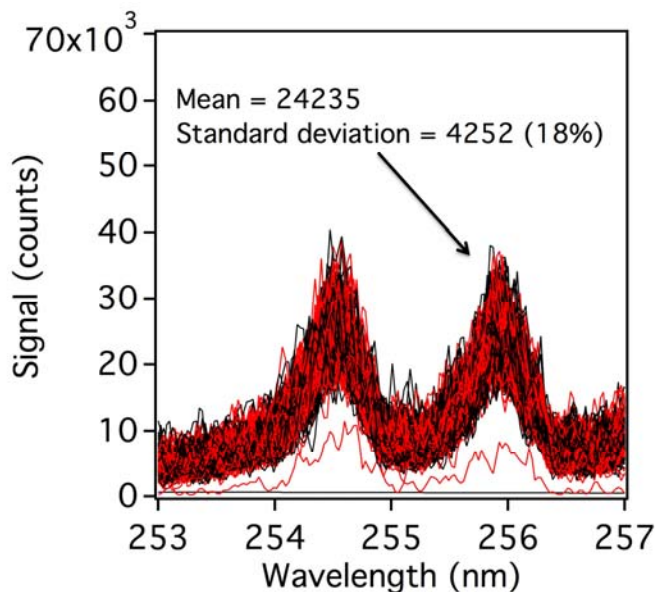

Figure 38 – Plot of 300 PF-LIF measurements made on a rotating sample in which DIPP was deposited on aluminum at a concentration of 74 μg/cm². The plot focuses on the region between 253 and 257 nm. Each spectrum was collected using a single pair of laser pulses. A 10X neutral-density filter was in place during the measurement to prevent saturation of the ICCD array. The mean and standard deviation of the 256-nm peak is indicated.

The measurement of Raman signal from an inkjet-deposited sample (280 μg/cm²) of DIPP on Al was also performed, yielding the results in Figure 39.   The data represent the integration of signal produced by 1000 pulses of 248-nm excitation having energies of 15 μJ/pulse (top left), 50 μJ/pulse (top right), and 100 μJ/pulse (bottom).   In this case, the sample was illuminated using an elliptically formatted (using a cylindrical lens) beam instead of the approximately circular focus that was used previously.   This was done in order to reduce the intensity of the laser on the surface in order to minimize its ablation. The long dimension of the illumination was sized so that it would not overfill the ICCD array – thus, all signal generated by the spot is integrated when the array is vertically binned.

 The results show that DIPP Raman is generated at all three energies, but that it becomes overwhelmed by ablative signals at 50 and 100 μJ/cm². At the lowest intensity, only DIPP Raman is observed. While the C-H stretch band near 3000 cm⁻¹ is strong, the other bands are in the noise. The signal is about 40% of that expected by scaling the results of Figure 36 for concentration, beam energy, and number of averages – this variance is within the bounds of uncertainty in the concentration produced by the airbrush. As the energy is

increased, apparent plasma emission is observed in both a broad-band and Al-line-emission form. Single-pulse PO LIF is also observed.

These and earlier data show that Raman measurements of OP agents can be hindered by inadvertant plasma generation on surfaces when lasers of high peak power are used. Similar observations were made by operators of fieldable Raman instruments [xxxix] at the Edgewood Chemical Biological Center.   The problem can be alleviated by reducing laser intensity, while still illuminating with a high photon dose, as the Raman signal will scale linearly with the total number of laser excitation photons deposited on the sample per integration period. Intensity can be reduced by spreading the beam to fill the viewing area of the spectrometer, and by increasing the laser pulse length.
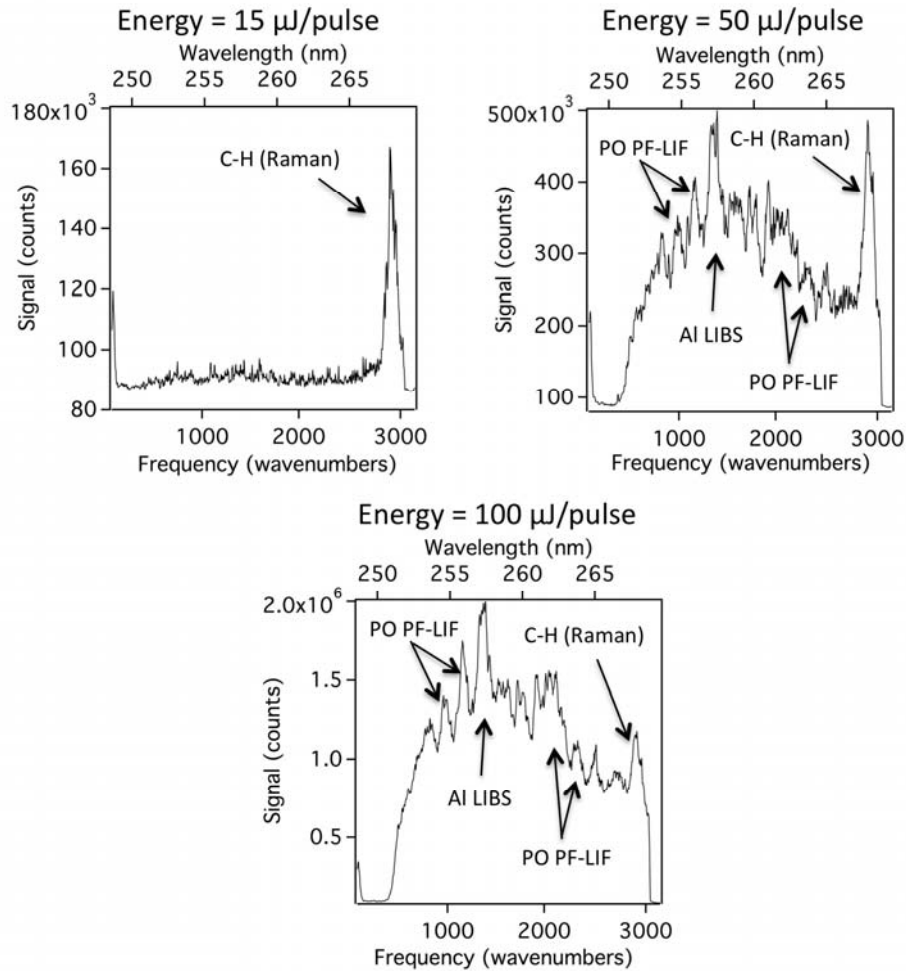
Figure 39 – Plot of the attempted Raman measurements of an inkjet-deposited DIPP on aluminum sample (280 µg/cm^2) as measured in Figure 38. In this case, only 248-nm excitation was used and the beam was elliptically formatted to illuminate most of the sample area viewed by the slit. The following pulse energies were used: top left: 15 µJ/pulse; top right: 50 µJ/pulse; bottom: 100 µJ/pulse. All represent the integration of 1000 shots of signal.

5.9.5 Raman detection of DIPP on concrete

The Raman detection of DIPP on concrete was also tested. The results are displayed in the left panel of Figure 40. Only samples created using the airbrush method were tested. Comparison of the measurements made on DIPP-coated (780 $\mu g/cm^2$) and uncoated concrete show that there was no evidence of a Raman signal under these conditions, even at the frequencies ($\sim$3000 cm^{-1}) of the strong C-H stretch. The concrete shows an apparent Raman signal that was present in some samples and not in others.

The right panel shows a PF-LIF spectrum measured on the same coated sample. The data were generated by integrating signal from 100 laser pulse-pairs while the signal was attenuated by 10X to avoid saturation of the ICCD. Both 0$\rightarrow$1 and 0$\rightarrow$2 spectral features are clearly evident.

It is likely that the Raman signal is not detected because most of the DIPP has diffused into the concrete surface where it is not visible. The PF-LIF measurement, on the other hand, is capable of penetrating the surface with the initial ablative pulse. This apparently releases PO from DIPP that is on or below the top concrete layer, and allows it to be detectable using LIF.
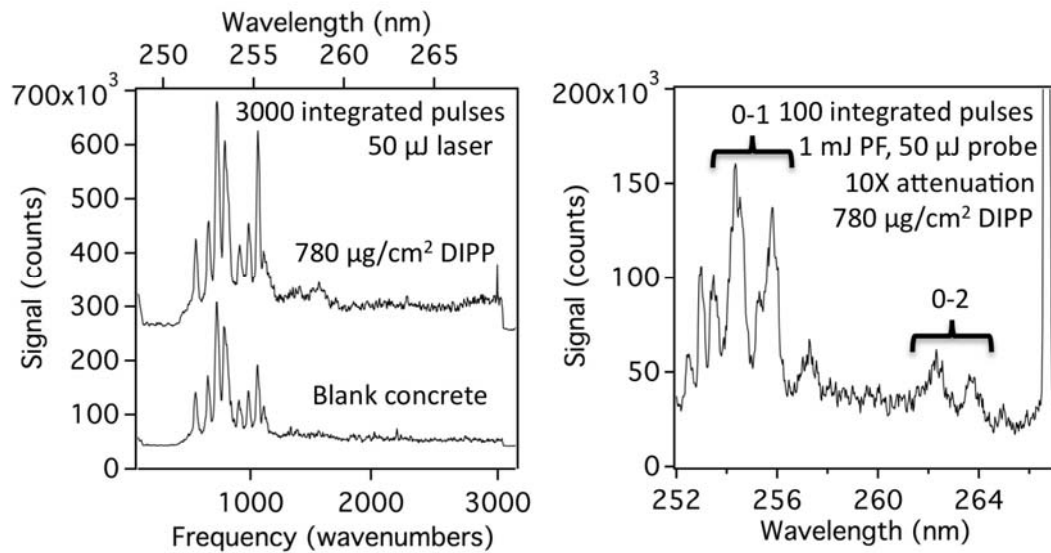

Figure 40 – <u>Left:</u> Raman spectra acquired from a concrete sample coated with 780 $\mu g/cm^2$ DIPP (top trace) and a blank concrete sample (lower trace); <u>Right</u>: PF-LIF spectrum of the same DIPP-coated sample.

6. CONCLUSIONS

This study has demonstrated the feasibility of using a two-pulse optical method to rapidly measure surface-borne OP contaminations at a sensitivity that is relevant to customer needs. It has focused on the specific application of low-volatility chemical agent sensing using a particular two-pulse approach (PF-LIF liberation and detection of the PO radical). Other two-pulse methods will likely be found that will couple other means of analyte disruption (e.g., evaporation or ionization) with other spectroscopic probes (e.g., absorption). If successful, these should have application in various security-related activities such as bioaerosol or nuclear material sensing.

The specific findings regarding operational PF-LIF detection of OP materials are listed as follows:

- PF-LIF was shown to detect all OP agent simulants (DMMP, DEMP, DIMP, DIPP) that were tested; thus, it is does not appear to be limited to a particular OP species.

- Detection was successful on all surface types tested – namely, concrete, wood, plastic, paper, painted steel, oxidized steel, and aluminum.

- Initial concerns that surface background fluorescence might strongly interfere with the measurement proved to be unfounded. Published [xix] observations that many natural and manmade surfaces produce low LIF backgrounds when excited and viewed in the deep UV (200-260 nm) appear to be accurate, at least for the materials tested here.

- The measured sensitivity for PF-LIF sensing of DIPP using a single pair (PF, probe) of laser pulses was 30 μg/cm^2 on an aluminum surface and 210 μg/cm^2 on concrete. The difference is a result of the fact that DIPP remains on an aluminum surface, while it diffuses into a porous concrete surface.

- The pulse energies required for the measurement are sufficiently low (0.5-1 mJ PF pulse; 25-50 μJ probe pulse) that a system could be implemented using commercial lasers with 1 kHz repetition rates. Thus, 1000 measurement points could be interrogated per second at the senstivies indicated above.

- The detection sensitivity can be improved by integrating signal over many pulses; the detection limit decreases in inverse proportion to the number of pulses integrated.

- When extrapolated to a 1 s response time (1000 integrated pulses) the performance was found to exceed that (3 μg/cm^2) desired by DHS for a scanned system by a large factor (14X for DIPP:concrete; 100X for DIPP:Al).

- When extrapolated to a 10 s response time, the performance fell short of that needed for the stringent EPA VX clearance level by 8X on Al and 58X on concrete. Extrapolation to a 580 s response time is required for detection at the clearance level for both Al and concrete. Such a long integration is not inconsistent with a clearance method, which currently requires offsite lab analysis. The validity of these extrapolations should, however, be tested.

- The measurement was found to produce false alarms from phosphate-containing materials, such as detergents, although the surface materials tested did not produce PO backgrounds.

- A logical implementation of the standoff PF-LIF method is as a rapidly scanned "trigger" for an identifier that would confirm or deny PF-LIF detections. A suitable identifier might be a mass spectrometer equipped with a DART or DESI interface, or it could be an optical measurement, such as Raman spectroscopy.

- Measurements of liquid films of DMMP, DIMP, DIPP, and phosphate soap were measured with Raman and it was concluded that all could be distinguished from one another using the Raman spectrum.

- The detection of DIPP on aluminum and concrete using Raman was tested. On aluminum, it was found to produce a signal 3260X weaker than that of PF-LIF. On concrete, a detectable signal was not measured at the concentration tested (780 $\mu g/cm^2$), presumably because most of it had diffused into the surface.

- The ability to make Raman measurements using pulsed lasers is limited to pulse energies below the ablative threshold. The detected Raman signal could be increased by using lower excitation intensities, which could be created by increasing the illuminated spot size on the sample, or by using longer pulse lengths or, even, continuous-wave laser illumination.

Some basic observations were also made regarding the specific mechanism of the PF-LIF process for OP detection, when implemented for surface detection:

- The laser intensities required for PF-LIF in the vapor phase are high enough to cause ablation of solid surfaces. The existence of a plasma appears to affect the dynamics and detection of PO in more than one way.

- Evidence exists that PO may be produced by recombination of atomized P + O in addition to, or instead of direct fragmentation. It is not possible to quantify the relative contribution of each at this time.

- While PO generated in vapor phase PF-LIF is rapidily (10's of ns) consumed by conversion to PO_2, it persists for a much longer time during a solid-phase PF-LIF measurement (optimal delay times for PO detection appear to be 0.6-1 μs after the PF pulse). It is possible that the dynamics of the $PO+O_2$ reaction are affected by the plasma:

  o Oxygen may be depleted in the plume, thus slowing the PO + O_2 reaction
  o If recombination is the dominant source of PO, it may occur slowly, thus causing a persistent source of PO that can be detected before the PO + O_2 reaction
  o PO may be generated by the probe pulse through disssociation of PO_2 and instantaneous excitation of PO LIF. This should also have been observed in prior studies that saw fast consumption of PO; however, it is possible that their probe intensity was not high enough to dissociate PO_2.

7. REFERENCES

i.   J. B. Simeonsson and R. C. Sausa, "A critical review of laser photo-fragmentation/fragment detection techniques for gas-phase chemical analysis," Appl. Spectrosc. Rev. **31**, 1-72 (1996).

ii. S. G. Buckley, C. S. McEnally, R. F. Sawyer, C. P. Koshland, and D. Lucas, "Metal emissions monitoring using excimer laser fragmentation fluorescence spectroscopy," Combust. Sci. and Tech. **118**, 169-188 (1996).

iii. B. L. Chadwick, G. Domazetis, and R. J. S. Morrison, "Multiwavelength monitoring of photofragment fluorescence after 193-nm photolysis of NaCl and NaOH - Application to measuring the sodium species released from coal at high-temperatures," Anal. Chem. **67**, 710-716 (1995).

iv. P. G. Griffin, R. J. S. Morrison, A. Campisi, and B. L. Chadwick, "Apparatus for the detection and removal of vapor phase alkali species from coal-derived gases at high temperature and pressure," Rev. Sci. Instrum. **69**, 3674-3677 (1998).

v.   P. Monkhouse, "On-line diagnostic methods for metal species in industrial process gas," Prog. Energy Combust. Sci. **28**, 331-381 (2002).

vi. R. C. Oldenborg and S. L. Baughcum, "Photofragment fluorescence as an analytical technique: Application to gas-phase alkali chlorides," Anal. Chem. **58**, 1430-1436 (1986).

vii. S. F. Rice, M. D. Allendorf, M. Velez, and J. M. Almanza, "Detection of NaOH vapor in glass furnaces using excimer laser photofragmentation spectroscopy," Glass Sci. Tech. **78**, 45-53 (2005).

viii.   A. A. Hoops and T. A. Reichardt, "Pulsed laser photofragment emission for detection of mercuric chloride," Appl. Opt. **45**, 6180-6186 (2006).

ix. T. Arusi-Parpar, D. Heflinger, and R. Lavi, "Photodissociation followed by laser-induced fluorescence at atmospheric pressure and 24°C: a unique scheme for remote detection of explosives," Appl. Opt. **40**, 6677-6681 (2001).

x.   C. Bauer, P. Geiser, J. Burgmeier, G. Holl, and W. Schade, "Pulsed laser surface fragmentation and mid-infrared laser spectroscopy for remote detection of explosives," Appl. Phys. B **85**, 251-256 (2006).

xi. G. M. Boudreaux, T. S. Miller, A. J. Kunefke, J. P. Singh, F. -Y. Yueh, and D. L. Monts, "Development of a photofragmentation laser-induced-fluorescence laser sensor for detection of 2,4,6-trinitrotoluene in soil and groundwater," Appl. Opt. **38**, 1411-1417 (1999).

xii. D. Heflinger, T. Arusi-Parpar, Y. Ron, and R. Lavi, "Application of a unique scheme for remote detection of explosives," Opt. Commun. **204**, 327-331 (2002).

xiii.   J. Shu, I. Bar and S. Rosenwaks, "NO and PO photofragments as trace analyte indicators of nitrocompounds and organophosphonates," Appl. Phys. B **71**, 665-672 (2000).

xiv. D. Wu, J. Singh, F. Yueh, and D. Monts, "2,4,6-Trinitrotoluene detection by laser-photofragmentation – laser-induced fluorescence," Appl. Opt. **35**, 3998-4003 (1996).

xv. S. R. Long, R. C. Sausa, and A. W. Miziolek, "LIF studies of PO produced in excimer laser photolysis of dimethyl methyl phosphonate," Chem. Phys. Lett. **117**, 505-510 (1985).

xvi. R. C. Sausa, A. W. Miziolek, and S. R. Long, "State distributions, quenching, and reaction of the PO radical generated in excimer laser photofragmentation of dimethyl methylphosphonate," J. Chem. Phys. **90**, 3994-3998 (1986).

xvii. C. M. Wynn, S. Palmacci, R. R. Kunz, K. Clow, and M. Rothschild, "Detection of condensed-phase explosives via laser-induced vaporization, photodissociation, and resonant excitation," Appl. Opt. **47**(31), 5767–5776 (2008).

xviii. K.N. Wong, W.R. Anderson, and A.J. Kotlar, "Radiative processes following laser excitation of the $A^2\Sigma^+$ state of PO", J. Chem. Phys. **85** 2406-2413 (1986).

xix. W.F. Hug, R. Bahartia, A. Tsapin, A. Lane, P. Conrad, K. Sijapati, R. D. Reid, "Water and surface contamination monitoring using deep UV laser-induced native fluorescence and Raman spectroscopy", Proc. of SPIE **6378**, 63780S (2006).

xx. S.R. Long, S.D. Christesen, A.P. Force, and J.S. Bernstein, "Rate constant for the reaction of PO radical with oxygen", J. Chem. Phys. **84** 5965-5966 (1986).

xxi. Bartelt-Hunt, S.L., D.R.U. Knappe, and M.A. Barlaz, "A review of chemical warfare agent simulants for the study of environmental behavior", Critical Reviews in Environmental Science and Technology 38(2): 112-136 (2008).

xxii. A.B. Butrow, J.H. Buchanan, and D.E. Tevault, "Vapor pressure of organophosphorus nerve agent simulant compounds" J. Chem. Eng. Data **54**, 1876-1883 (2009).

xxiii. Manufacturer's database – Sigma Aldrich.

xxiv. M. Baudelet, M. Boueri, J. Yu, S.S. Mao, V. Piscitelli, X. Mao, and R.E. Russo, "Time-resolved ultraviolet laser-induced breakdown spectroscopy for organic material analysis", Spectrochim. Acta Part B 62, 1329-1334 (2007).

xxv. National Institute of Standards and Technology (NIST) Atomic Spectra Database – www.nist.gov/pml/data/asd.cfm

xxvi. A. Metropoulos, A. Papakondylis, and A. Mavridis, "Ab initio investigation of the ground state properties of PO, PO^+, and PO^-", J. Chem. Phys. **119**, 5981-5987 (2003).

xxvii. H.R. Griem, Plasma spectroscopy, New York, NY, McGraw-Hill, 1964.

xxviii. W.T.Y. Mohamed, "Fast LIBS identification of aluminum alloys," Prog. in Phys. **2**, 87-92 (2007).

xxix. A. A. Hoops, T. A. Reichardt, D. A. V. Kliner, J. P. Koplow, S. W. Moore, "Detection of mercuric chloride by photofragment emission using a frequency-converted fiber amplifier," Appl. Opt. **46**, 4008-4014 (2007).

xxx. C. D. Brown and H. T. Davis, "Receiver operating characteristics curves and related decision measures: A tutorial," Chemom. Intell. Lab. Syst. **80**, 24-38 (2006).

xxxi. C. G. Fraga, A. M. Melville, and B. W. Wright, "ROC-curve approach for determining the detection limit of a field chemical sensor," Analyst **132**, 230-236 (2007).

xxxii. J. M. Headrick, T. A. Reichardt, T. B. Settersten, R. P. Bambha, and D. A. V. Kliner, "Application of laser photofragmentation-resonance enhanced multi-photon ionization to ion mobility spectrometry," Appl. Opt. **49**, 2204-2214 (2010).

xxxiii. M. C. Pedroso, M. B. Sinclair, H. D. T. Jones, and D. M. Haaland, "Hyperspectral confocal fluorescence microscope: A new look into the cell," Microscopy Today, September 2010, pp. 22-25.

xxxiv. Don Bansleben, DHS, Donald.Bansleben@dhs.gov

xxxv. Battelle, "Testing and Quality Assurance Plan for the Evaluation of Wipe Sampling Methods for Collecting Chemical Warfare Agents (CWAs), CWA Degradation Products, and Toxic Industrial Chemicals from Various Surfaces", US Environmental Protection Agency Report EPA/600/R-08/079, February, 2008.

xxxvi. R. B. Cody, J.A. Laramee, and H. Dupont Durst, "Versatile new ion source for the analysis of materials in open air under ambient conditions", Anal. Chem. **77**, 2297-2302 (2005).

xxxvii. I. Cotte-Rodriguez and R. Graham Cooks, "Non-proximate detection of explosives and chemical warfare agent simulants by desorption electrospray ionization mass spectrometry, Chem. Commun., 2006, 2968-2970.

xxxviii. P. Ponsardin, S. Higdon, T. Chyba, W. Armstrong, A. Sedlacek, S. Christiesen, and A. Wong, "Expanding applications for surface-contaminants sensing using the laser interrogation of surface agents (LISA) technique" Proc. SPIE **5268**, 321-327 (2004).

xxxix. Darren Emge, ECBC, private communication.